

RESEARCH

Open Access



Structural Behavior of a Laterally Restrained Precast Reinforced Concrete Arch Deck Under Punching Shear Loading

Dal-Hun Yang¹, Seung-Jai Choi², Sung-Jae Kim³ and Jang-Ho Jay Kim^{2*} 

Abstract

In the construction of concrete bridges, the lighter dead load of decks can significantly reduce the number or size of substructure members, such as girders, piers and foundations. Although, the arch decks (ADs) ensure superior load carrying capacity and can have longer span length than flat decks (FDs), relatively minute number of studies was performed on longer span decks manufactured as arch shape to maximize the performance. In the previous study, a precast reinforced concrete (RC) AD with enhanced width of 2.5 m was developed. In this study, the behavior of precast RC AD under punching shear load was studied. Three real-scale AD specimens were tested and analyzed to understand its performance under punching shear loading. Different sizes of the ADs were manufactured to evaluate the punching shear capacity. The punching shear capacity and failure mode were obtained from the test, and the results were then compared to various design provisions. Finite Element Analyses (FEAs) were conducted to validate the experiment results and to verify the arching action of the AD with various thicknesses. The study results clearly verified that the AD had a higher or similar load-carrying capacity than the FD due to the arching action caused by the lateral restraint and arch shape, despite of thinner thickness of AD than FD. An analytical and prediction model for the punching shear behavior of ADs was developed and calibrated. The resulting models are described in a code-friendly formulation.

Keywords: arch deck, precast concrete deck, punching shear, arching action, structural behavior, structural analysis

1 Introduction

Since the construction cost is the most important factor in current bridge construction projects, the minimization of bridge superstructure member (i.e., girders, decks, etc.) is the main factor in reducing construction cost and time. For example, the prestressed concrete (PSC) construction method has been used to widely in bridge construction since 1960s to increase the longitudinal length of girder to reduce construction cost, as shown in Fig. 1 (Ministry of Land, Infrastructure and

Transport (MOLIT), 2020). The increase in span length would reduce required substructures construction, such as piers, bearing, and foundation. However, until now, bridge deck width improvement has not been attempted as much as a girder span lengthening due to the possibility of punching shear failure problem that may occur in wider bridge decks. However, the bridge deck is most affected directly by dynamic vehicle loading in bridge superstructure member, the attempt to widen the bridge deck has not been attempted until now. However, the growing demands of wider span decks with sufficient stiffness to have good punching shear resistance to reduce construction cost. The present bridge decks have relatively short span length of (1.5–2.0 m) due to commonly used cast-in-place (CIP) construction method and flat cross-sectional shape. To overcome these limitations,

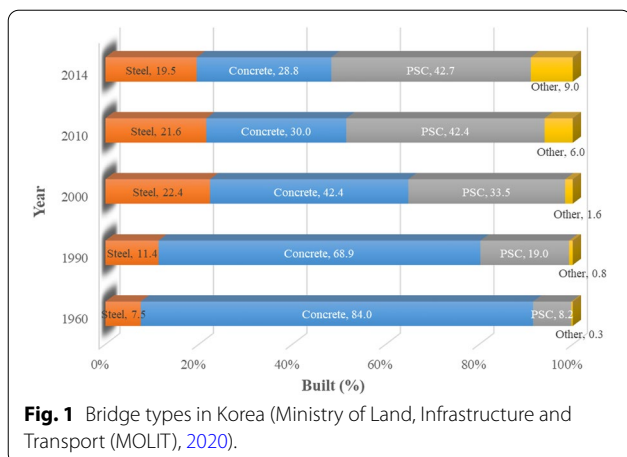
Journal information: ISSN 1976-0485 / eISSN 2234-1315

*Correspondence: jhkim@yonsei.ac.kr

² School of Civil and Environmental Engineering, Yonsei University, 50, Yonsei-ro, Seodaemun-gu, Seoul 03722, Republic of Korea
Full list of author information is available at the end of the article



© The Author(s) 2022. **Open Access** This article is licensed under a Creative Commons Attribution 4.0 International License, which permits use, sharing, adaptation, distribution and reproduction in any medium or format, as long as you give appropriate credit to the original author(s) and the source, provide a link to the Creative Commons licence, and indicate if changes were made. The images or other third party material in this article are included in the article's Creative Commons licence, unless indicated otherwise in a credit line to the material. If material is not included in the article's Creative Commons licence and your intended use is not permitted by statutory regulation or exceeds the permitted use, you will need to obtain permission directly from the copyright holder. To view a copy of this licence, visit <http://creativecommons.org/licenses/by/4.0/>.

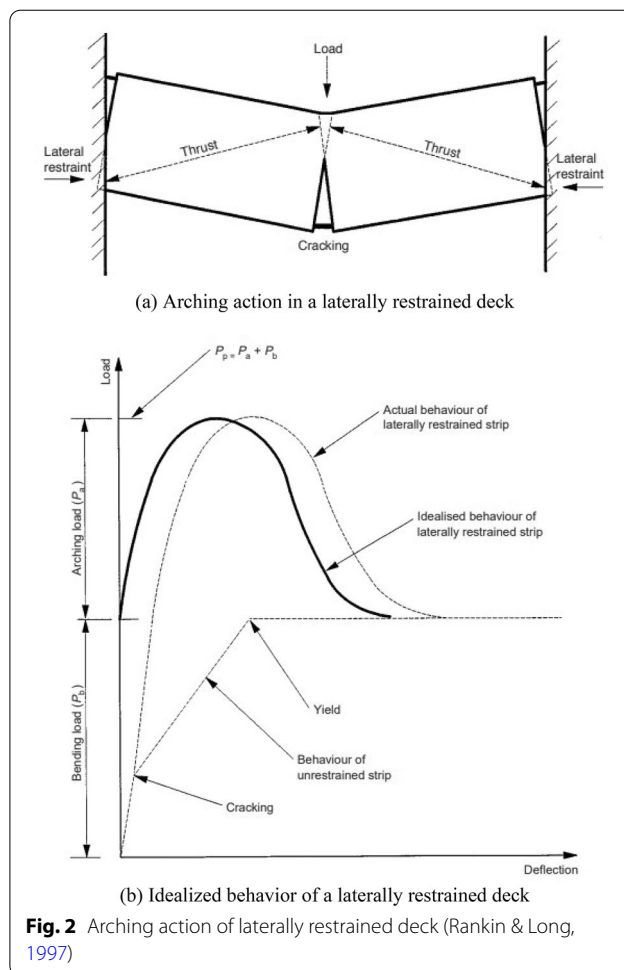


arch shaped prefabricated deck is proposed in this study to increase the bridge deck width. Arch shaped concrete members principally resist load predominantly through compressive stresses, which is an ideal load-carrying method for members constructed using tensile cracking prone material, such as concrete. Therefore, arch structures are historically used to construct longer span required structural members such as cathedral roofs, bridges, and etc. constructed using rock and unreinforced concrete (Au et al., 2003; Fanning & Boothby, 2001; Ohura & Kato, 1993; Oldrieve, 1915).

Recently, many bridge engineers desire to improve the deck width using better load-transfer mechanism (Kang & Tan, 2016; Wang et al., 2019; Yu and Tan, 2014). As shown in Fig. 2a, b, Rankin and Long (1997) studied the flexural and shear capacity of decks by enforcing predominant compressive membrane action (arching action) using the lateral restraints applied to the supports. Using the precast RC arch deck (AD), the span length exceeding 2.0 m was achieved using this load-transfer mechanism. Based on the study result, the application of arching action to the RC bridge deck seems to be possible by delaying its flexural and punching shear failure.

2 Research Significance

The most critical loads to the bridge decks is from the vehicle dynamic load. Since the vehicle load is concentrated at the certain areas of the deck surface, the repetitious load would cause localize failures at the area. Since the bridge deck thickness is relatively thin compared to the width and length of the deck, the most common failure comes from the punching shear stresses. Therefore, extensive investigations have been performed on to understand the punching shear capacity for its resistance under dynamic vehicle load.



Many researchers have studied to understand on arching action effect on the load-carrying capacity and the confinement of bridge decks. There have been numerous research reports showing that arching action greatly improve the punching shear capacity. Keyvani et al. (2014) analytically studied punching shear behavior of laterally restrained RC flat decks (FDs) with compressive membrane action (arching action). They found that the arching action helped resist progressive collapse. Arshian and Morgenthal (2017) also investigated the load-carrying capacity in laterally restrained two-way RC FDs using probabilistic approaches. They found that the strength enhancement due to arching action increases with the increase in the relative rebar ratio. Thus, larger arching depth and, in turn, higher arching moment would be expected. Amir et al. (2016) also reported the test results on punching shear behavior of a laterally restrained PSC FDs. They found that as a result of arching action by virtue of lateral restraint effects, in combination with the transverse prestressing, the punching shear resistance of

the decks was much larger than predicted by most international codes that do not consider the effect of CMA. Peng et al. (2017) verified the arching action of laterally restrained FDs based on empirical formulas and design codes. Their experiments indicated that, under the level of restraint achieved in the tests, the arching action could enhance the punching resistance by as much as 9.5%. However, these studies and design codes are focused on only laterally restrained supports, which is related arching action.

There is no available experimental and theoretical works have performed on laterally restrained AD. It is expected that arching action enhancement of laterally restrained AD than laterally restrained FD, as shown in Fig. 3a–d. However, since the study have not performed the load test of AD has not been performed to understand on arching action effect on the punching shear capacity, the test and simulation to require the detail behavior of the arching action in AD. Therefore, in this paper, three real-scale testes of a laterally restrained precast AD under punching shear loading are performed to investigate its structural behavior. The precast AD specimens section are shown in Fig. 4a–c and the dimensions of the test specimens of AD are shown in Fig. 4d–f.

3 Previous Research for Flexural Behavior of Arch Deck

In the previously published report by Yang et al. (2018), the flexural behavior of precast RC AD with 2.5 m span length was discussed. The results from flexural tests showed that the precast RC AD provides flexural capacity superior to that of a conventional flat deck. Yang et al. (2018) verified that the static loading tests of SSAD (Static load testing of Single Arch Deck) and SCAD (Static load testing of Composite Arch Deck) showed superior flexural behavior of the AD. As shown in Fig. 5a, b, the average maximum load of SSADs was 64.48 kN, which is equivalent to approximately 1.7 times the design load ($P_{r,ssad}$) 37.12 kN, as specified by the Korean Highway Bridge Design code (KHBD) code (Limit state design 2015). The failure load of the SCAD was 922.80 kN, which is approximately 2.4 times the design load of ($P_{r,scad}$) 384.31 kN, showing that the load carrying capacity of the AD was much higher than that of the FD. Overall analytical results were very similar to the test results; however, the initial stiffness of SCAD from the simulations was slightly higher than that of test. If more SCAD specimens were tested, it is expected that the test and simulation deviation would nearly be equivalent. Through the experimental and simulation result comparison, the superior flexural performance of SSAD and SCAD due to better load transfer mechanism from arching action (or compressive membrane action) was verified. Also, the

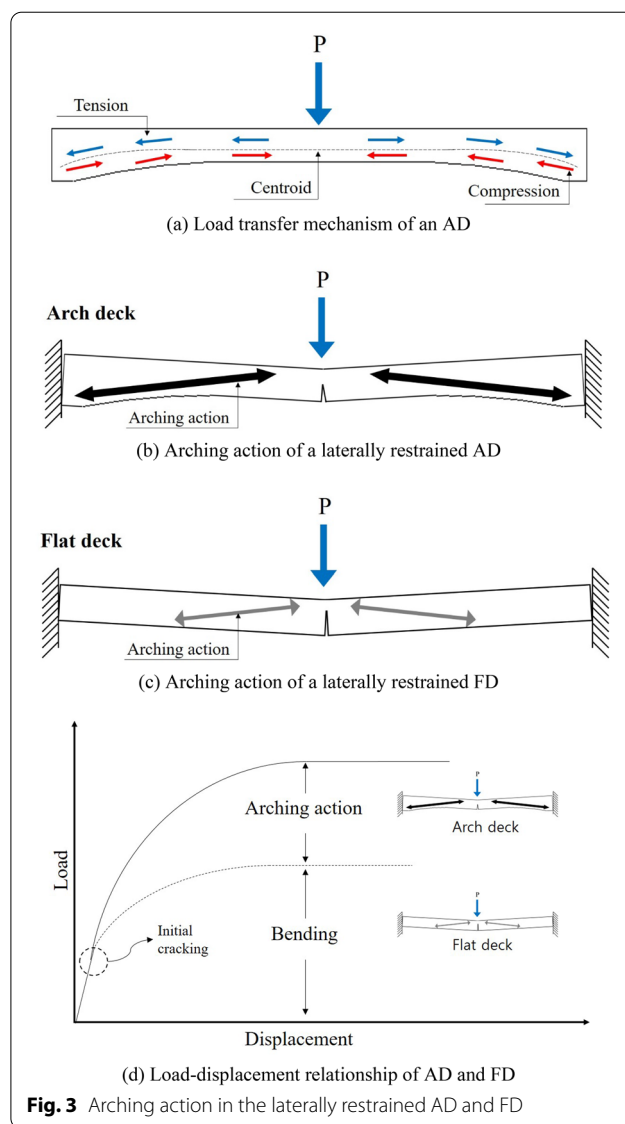


Fig. 3 Arching action in the laterally restrained AD and FD

results showed that the initial cracking and ultimate failure occurred at loads greater than the design calculated loads. Based on the previous research results, the structural behavior of a laterally restrained precast RC arch deck under punching shear loading is investigated in this study. This study is conducted to apply RC bridge decks for actual medium-to-long span PSC bridge construction. Fig. 6 shows the flowchart of this study.

4 Punching Shear Test Investigation

4.1 Design of the Specimen

Four standard ADs and one square AD (length and width of 2.5 m) were manufactured to construct the composite structures. Then, AD and square AD were placed and connected to concrete girders. For rebar connections

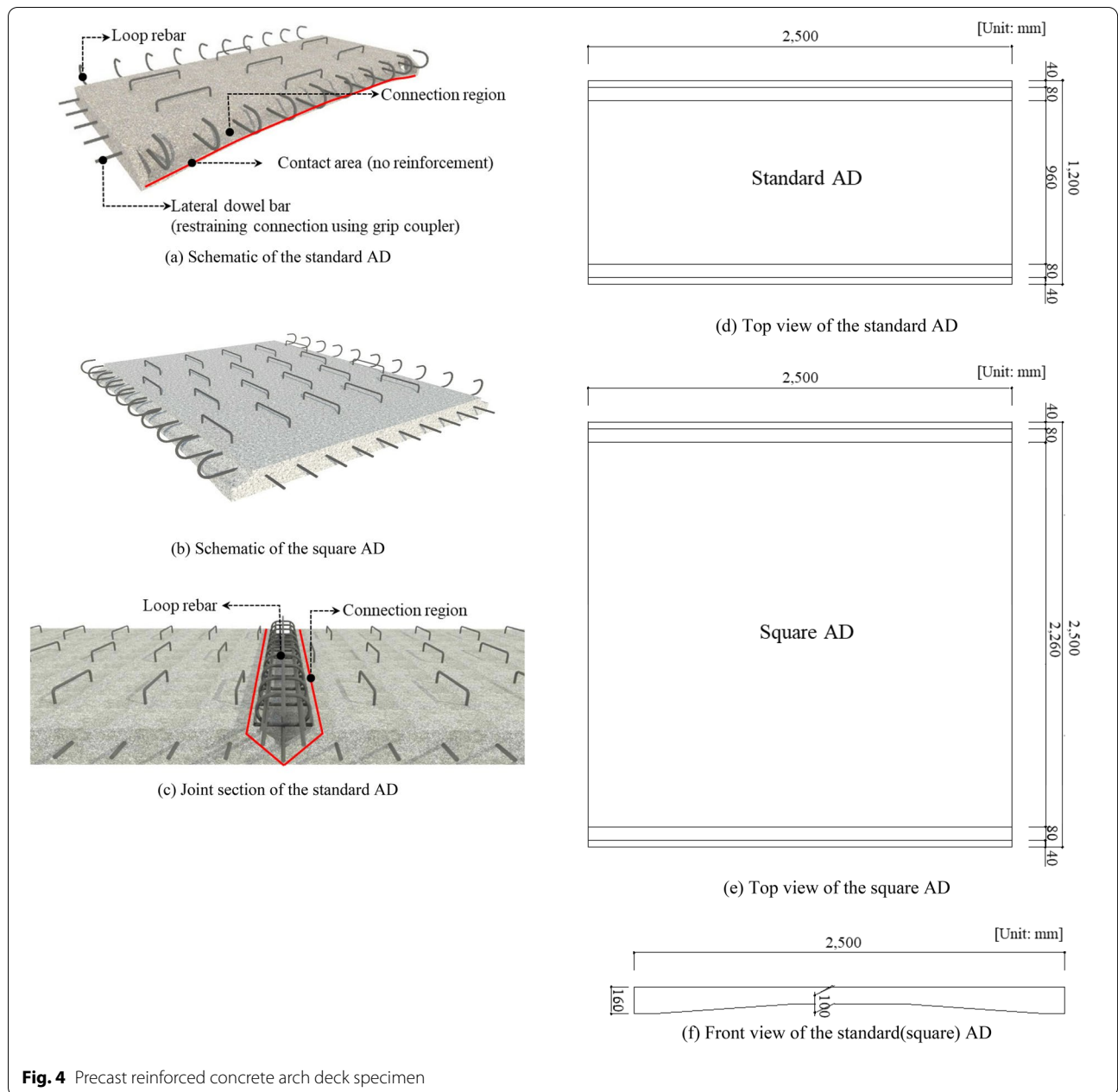


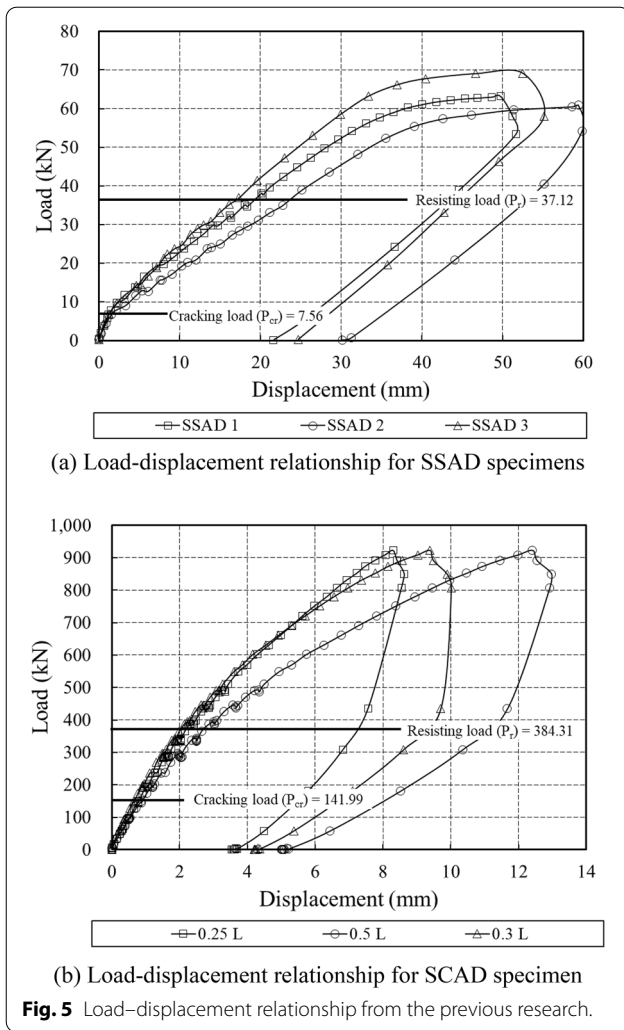
Fig. 4 Precast reinforced concrete arch deck specimen

between AD and girder, a grip coupler was used. Then a cast-in-place (CIP) overlay concrete was casted, and steam cured to develop sufficient early age concrete strength. Fig. 7a–h shows the fabrication process of the specimens. The composite specimens with two ADs for punching shear test were titled as PCAD (Punching shear testing of Composite Arch Deck) 1(1–1 and 1–2). The name of the composite specimen with one square AD was PCAD 2. The material properties of PCADs were as same as those of specimens used in the previous study, as shown in Table 1. All specimens were casted using OPC

(ordinary Portland concrete) with coarse aggregate maximum size of 25 mm. The 28 day concrete compressive strength of SSAD and cast-in-place (CIP) overlay concrete were 49.5 and 38.5 MPa, respectively. SD400 rebars with manufacturer specified minimum yield strength of 400 MPa were used for reinforcements.

The design values for this test were taken from the KHBD code. The design punching shear service strength $V_{ser,khbd}$ is given by the following equation:

$$V_{ser,khbd} = P \times LL \times IM \tag{1}$$



where P is the maximum wheel load of the truck (DB-24), LL is the live load coefficient, IM is the impact coefficient.

The design punching shear strength $V_{u,khbd}$ was calculated using the following equation:

$$V_{u,khbd} = v_u \times u_i \times d \tag{2}$$

where u_i is the perimeter of the critical section, d is the average effective depth of deck, v_u is the punching shear stress equation shown in the following equation:

$$v_u = 0.85\phi_c k (100\rho_l f_{ck})^{1/3} + 0.10f_n \geq (0.4\phi_c f_{ctk} + 0.10f_n) \tag{3}$$

where ϕ_c is the material coefficient of concrete, k is $1 + \sqrt{200/d} \leq 2.0$, ρ_l is longitudinal rebar ratio, f_{ck} is the compressive strength of concrete, f_n is the orthogonal stress in cross section, f_{ctk} is the tensile strength of concrete.

In addition, the design punching shear load of ACI 318 and Eurocode 2 were calculated and compared. The design punching shear strength $V_{u,aci}$ and $V_{u,ec2}$ are shown in Eqs. (4) and (5), respectively:

$$V_{u,aci} = 0.17(1 + \frac{2}{\beta})\sqrt{f'_c}bd \tag{4}$$

where β is the ratio of the long side to the short side for the loading area, f'_c is the compressive strength of concrete, b is the perimeter of critical section and d is the average effective depth of deck:

$$V_{u,ec2} = 0.12k(100\rho_f f'_c)^{1/3}u_1d \tag{5}$$

where k is $1 + \sqrt{200/d} \leq 2.0$, ρ_f is the ratio of flexure reinforcement, f'_c is the compressive strength of concrete, u_1 is the perimeter of critical section, d is the average effective depth of deck.

4.2 Performance Evaluation of the Grip Couplers

In this study, the transverse rebars of the AD and supporting girders were connected using a grip coupler to restrain the transverse direction (Fig. 7d, e). The rebar was restrained with a steel pipe sleeve, which was compressed using a hydraulic compressor, thus shortening the construction time. To verify the performance of the grip couplers, various types of SD400 rebar (H16, 19, 22, 25, 29, and 32) with a yield strength of 400 MPa and an ultimate strength of 560 MPa were employed for each specimen. Axial tensile tests were performed to confirm that the tensile strength of the grip coupler is greater than the tensile strength of the rebar, so all specimens break at the rebar section. All of the conducted tests satisfied these criteria, and the results are shown in Table 2 and Fig. 8a–f.

4.3 Punching Shear Test Setup and Procedure

The specimen and test setup of the PCAD 1 and 2 are shown in Fig. 9a–e, respectively. The specimen was supported on two supporting steel girders spaced at 2500 mm from end-to-end, and rubber pads were placed between the specimen and girder. Two steel I-beams were supported at front and rear side to induce the punching shear stress. The spacing along the lateral direction for the installation of LVDTs and cracking monitoring on the bottom of the specimen during the punching shear loading test is shown in Fig. 9a. The specimen was bolted to the top flange of the I-girders through two rows of holes

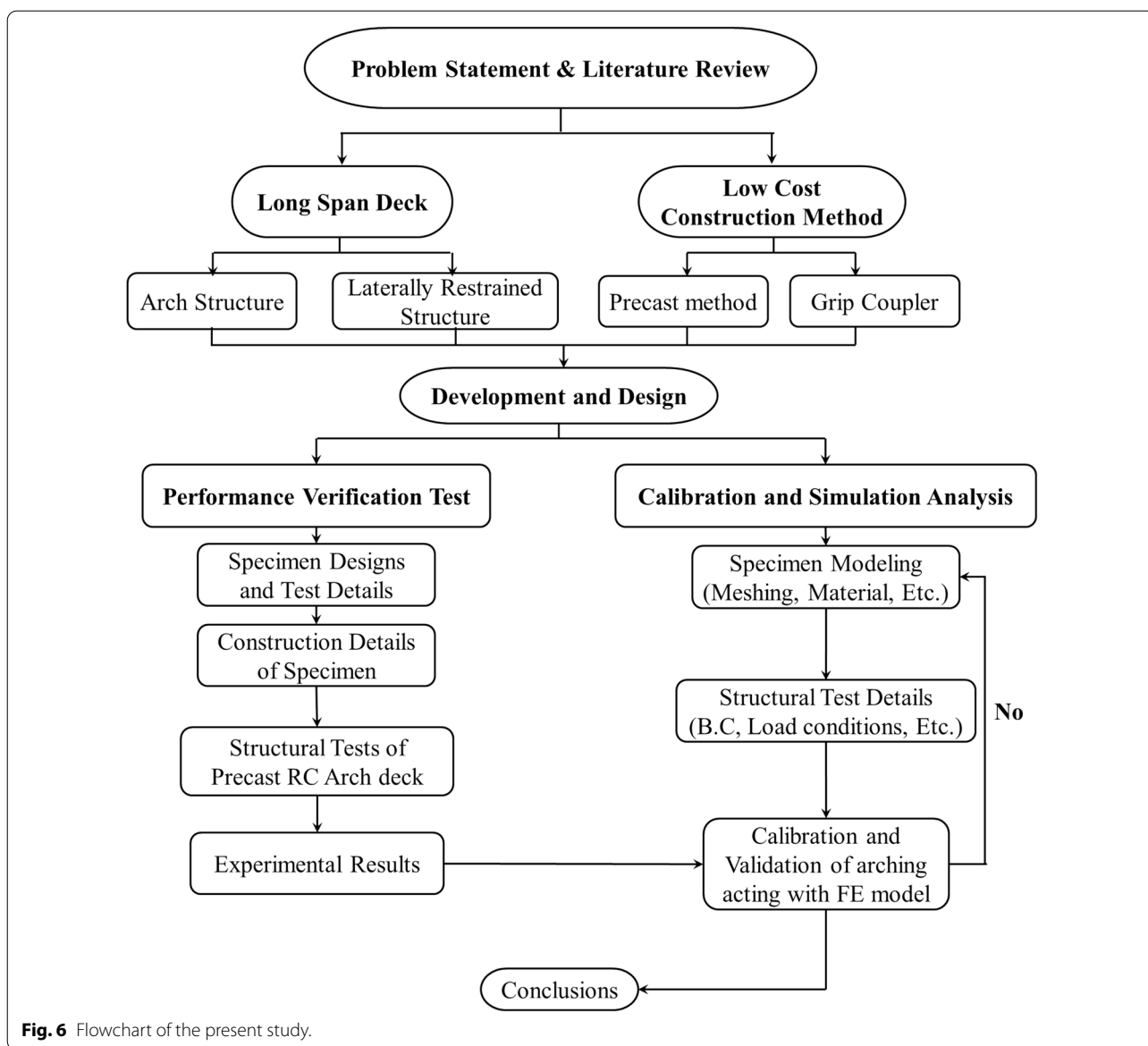


Fig. 6 Flowchart of the present study.

at each sides using 25 mm diameter steel bolts to prevent any lateral and vertical movement of the decks.

The instrumentation and loading area are shown in Fig. 9b–d. Three LVDTs were installed perpendicularly to measure the deflections at 0.5L, 0.33L and 0.25L locations of the lateral length (2500 mm) of AD. Electrical strain gauges were used to measure strains in rebars and concrete surface at 0.5 L, 0.33 L and 0.25 L along the lateral length of AD. In addition, one Ω shape strain type displacement transducers (STDT) were attached to the bottom surface of AD central joint section and bottom critical section of square AD. The loading was provided using a 5000 kN capacity hydraulic actuator located at the center of the specimen to simulate the effect of

punching shear induced by the truck wheel load, as shown in Fig. 9e. A 230 × 580 mm steel plate with a thickness of 30 mm was used to transfer the loads from the actuators to comply with the LSD specified by the KHBD code for a contact loading area. The loading area A_p can be calculated using the following equation:

$$A_p = \frac{12,500}{9} P(mm^2) \tag{6}$$

where P is 96 kN, which is first class bridge vehicle wheel load requirement (DB-24) in KHBD. The ratio of width to length was 1–2.5 with a steel plate dimension of a width 230 mm and a length of 580 mm.



Fig. 7 Fabrication process for the PCAD specimens

The loading sequence of the test had three steps, as shown in Table 3. The first step had a loading rate of 0.1 mm/min from 0 to 300 kN, the second step had a loading rate of 0.2 mm/min from 300 to 650 kN, and the third step had a loading rate of 0.5 mm/min from 650 to P_u . The cracks on the bottom surface were monitored and marked at intervals of 50 kN from 300 to 700 kN.

5 Punching Shear Test Results

Ultimate load, cracking pattern, failure mode, load–deflection curve, and load–strain curve results are presented in this section. A summary of the test results is provided in Table 4. The design punching shear service load V_{ser} was taken as 303.75 kN, and the design

punching shear strength $V_{u,khbd}$ was taken as 746.10 kN calculated from Eqs. (1) and (2), respectively.

5.1 Punching Shear Capacity

The yield and ultimate loads of all specimens were observed to be higher than the design punching shear service load and design punching shear load, respectively. The average ultimate loads for PCAD 1 and 2 were 792.4 and 819.5 kN, respectively, which is approximately 1.06 and 1.1 times higher than the design punching shear strength (746.1 kN), respectively. From the previous test results, the PCAD specimens exhibited a greater structural capacity than the conventional FD specimens. PCAD 1–2 and PCAD 2 produced similar results, but the average structural capacity of PCAD 1–1 and 1–2 was lower than that of PCAD 2. The two ADs in PCADs



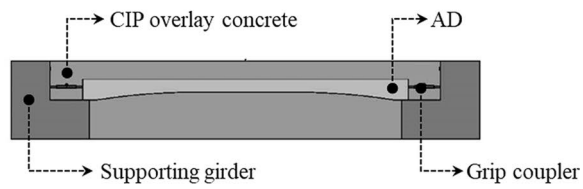
(g) Square AD



(h) Upper rebar assembly



(i) Cast-in-place (CIP) overlay concrete casting



(j) Schematic of the PCAD specimens

Fig. 7 continued

Table 1 Material properties of the specimens (Unit: MPa).

Material	Member	Strength	Type
Concrete	Arch deck	49.5	OPC
	CIP	38.5	
Reinforcing bar	–	400	SD400

1–1 and 1–2 were connected by reinforcing bars, but the square AD in PCAD 2 consisted of a single member, so the stiffness was slightly different. However, there was no significant difference in the ultimate load and maximum displacement between PCAD 1–2 to PCAD 2. Therefore, it can be assumed that, if a larger number of PCAD 2 specimens was tested, the performance difference between the two specimen types would be lower based on the average results.

5.2 Crack Patterns

The initial cracks in PCAD 1–1, 1–2 and 2 occurred on the bottom surface of the deck at 300, 350, and 350 kN, respectively, at loads approximately 1.15–1.48 times higher than the design punching shear service load of 303.75 kN. Fig. 10a–d presents the crack patterns in each specimen according to the load. As expected, the flexural cracks occurred at the early stages of the loading, and radial cracks gradually occurred from the center as the load increased. Initially, PCAD 1 mainly exhibited flexural cracks due to the separation of the AD joints, while PCAD 2 had more cracks than PCAD 1. The square AD had no joints and had larger crack widths than the standard ADs. As the load increased, radial cracks instead of flexural cracks mainly occurred in both PCADs 1 and 2. The final crack pattern can be characterized by radial crack propagation in both PCADs 1 and 2.

5.3 Load–displacement Behavior

Fig. 11a–d presents the load–displacement relationship for the PCAD specimens. The load–displacement curves were bi-linear, with the inflection point at approximately

350 kN, which can be tributed to cracking and joint separation loading to a significant reduction of the tensile resistance of concrete, where the reinforcements resisted most of the tensile stresses. In addition, from the initial load to 350 kN, all of the specimens exhibited similar linear elastic behavior. At approximately 350 kN, the slopes of the load–displacement curves for the specimens changed, reflecting its inelastic behavior. The displacement of PCAD 1 increased dramatically, unlike that of PCAD 2, which is a reflection of the difference between the standard AD used in PCAD 1 and the square AD used in PCAD 2. The rapid increase in displacement of PCAD 1 was likely due to the separation of the connection joints of the two AD. However, the displacement in PCAD 2 slowly increased with cracking at the center of the square AD. In the 350–650 kN range of the specimen, cracking occurred rapidly causing the displacement to increase. At the loads higher than 650 kN, the displacement increased significantly due to the reduction in stiffness caused by rebar yielding. At this point, the load dropped suddenly, and the area around loading showed crushing, indicating that punching shear failure had occurred. At approximately 800 kN, the ultimate load was reached with a maximum displacement of 15.54, 14.80, and 13.02 mm for PCAD 1–1, 1–2, and 2, respectively. The displacement at 0.33 L and 0.25 L were approximately 7–30% and 40–50% lower than the maximum displacement (0.5 L), respectively.

5.4 Load–Strain Behavior

The strain test results in the central rebar and the top surface of the concrete around the loading area are shown in Fig. 12. The rebar used in the PCAD specimens was SD400, with a yield and ultimate strength of 400 and 560 MPa, respectively. When the strain in the rebar exceeded 2000 $\mu\epsilon$, yielding behavior was exhibited, while at a strain exceeding 2800 $\mu\epsilon$, the strain hardening behavior was observed, reflecting the service limit state of the structure. Similar behavior was observed for the PCAD 1–1, 1–2 and 2 test

Table 2 Axial tensile test results of the grip coupler.

Index	Area (mm ²)	Yield strength (N/mm ²)	Ultimate strength (N/mm ²)	Breaking point	Decision
H16	198.6	448.1	680.8	Rebar	OK
H19	286.5	420.0	617.7	Rebar	OK
H22	387.1	516.7	658.1	Rebar	OK
H25	506.7	462.4	613.6	Rebar	OK
H29	642.4	446.0	584.2	Rebar	OK
H32	794.2	425.0	575.9	Rebar	OK
Criterion	–	–	560	Rebar	OK

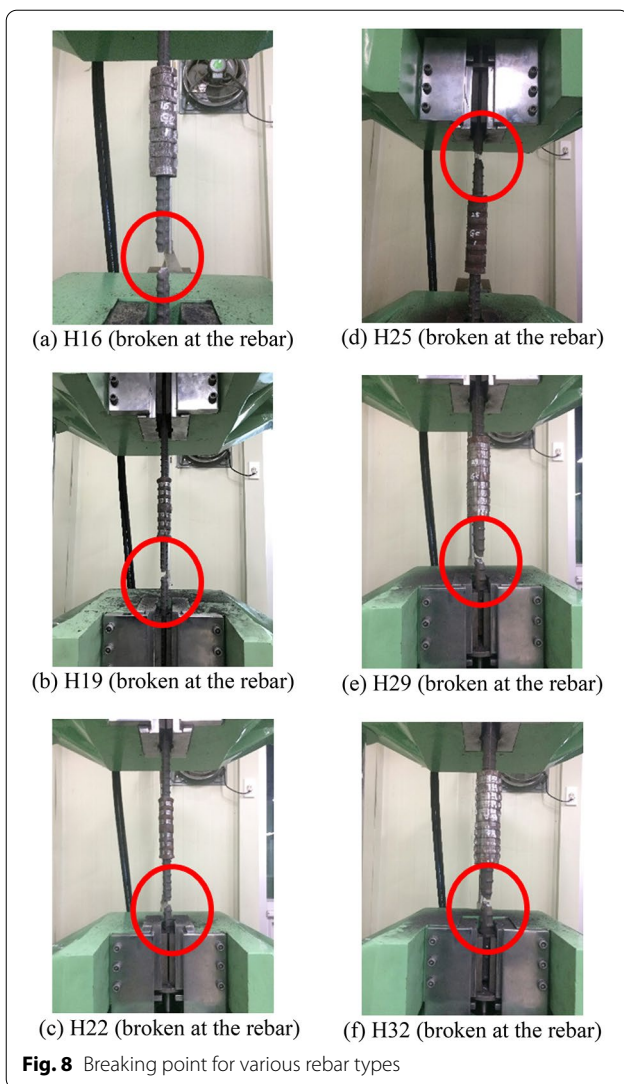


Fig. 8 Breaking point for various rebar types

results from 0 to 700 kN. After 700 kN, the strain in PCAD 1–1 and 1–2 increased slowly, while the strain in PCAD 2 increased rapidly. That is, it is important to note that the strain hardening behavior of PCAD 1 and 2 occurred at approximately 2500 and 2000 $\mu\epsilon$, respectively. These strain trends can be explained in two ways. First, the development of arching action according to the longitudinal and transverse rebar ratios of the ADs is due to the arch shape in the transverse direction, while a flat shape in the longitudinal direction. Standard AD has a dimensional ratio of 1:2 in longitudinal and transverse directions, and has an arch dominant cross section. However, square AD has a dimensional ratio of 1:1 in longitudinal and transverse directions, and has relatively less arch shape compared to standard AD. Zheng et al. (2012) stated that rupture of rebar did

not occur due to the arch action. Also, due to the development of arching action, the strain hardening behavior could be delayed in PCAD 1 compared to PCAD 2 (a specimen with less arching action). Therefore, confirming indirectly that the lateral stiffness is higher than that of the flat deck or laterally unrestrained deck. Second, loop rebar was used in PCAD 1 in the joint connection, while square AD had no joint. Due to the joint difference in the two specimens, square AD showed a higher strain than standard AD due to larger rebar ratio in standard AD.

The concrete strain also exhibited bi-linear curves with a slope change occurring at the initial cracking of the concrete. At the design service load, the concrete strain in PCAD 1–1, 1–2, and 2 was -327 , -188 , and $-266 \mu\epsilon$, respectively. The ratio of the strain at design service load to the strain at failure of PCAD 1–1, 1–2, and 2 was approximately 29, 10, and 27%, respectively.

5.5 Joint Behavior

The load-joint separation displacement relationship measured using an STDT is shown in Fig. 13. Joint separation in PCADs 1–1 and 2 occurred gradually from the beginning of the test, due to the inherent precast AD characteristic, and the opening of the joint due to macro-cracks and the applied load. In contrast, PCAD 2 initially had a gap width of close to 0, but this increased after 250 kN and 350 kN due to the micro-crack formations and the macro-crack propagations, respectively. After 350 kN, the crack width gradually increased. The joint separation displacement for PCADs 1–1, 1–2, and 2 at the design punching shear strength of 746.1 kN was 1.21, 1.25, and 1.11 mm, respectively.

6 Analytical Validation

6.1 Numerical Modeling

The precast RC arch decks subjected to punching shear load were simulated using MIDAS FEA, a commercial finite element analysis program co-developed by MIDAS IT and TNO DIANA, purposely designed for advanced nonlinear detailed simulations of concrete structures. The quasi-static simulation using MIDAS FEA was performed for all specimens. It should be noted that constitutive model, element mesh, and boundary conditions (BCs) were previously calibrated and validated in the previous study results (Yang et al., 2018). In this study, a total strain crack (TSC) model, which is based on smeared crack approach, is used for the concrete constitutive model. The constitutive model based on total strain is developed along the lines of the Modified Compression Field Theory, originally proposed by Vecchio

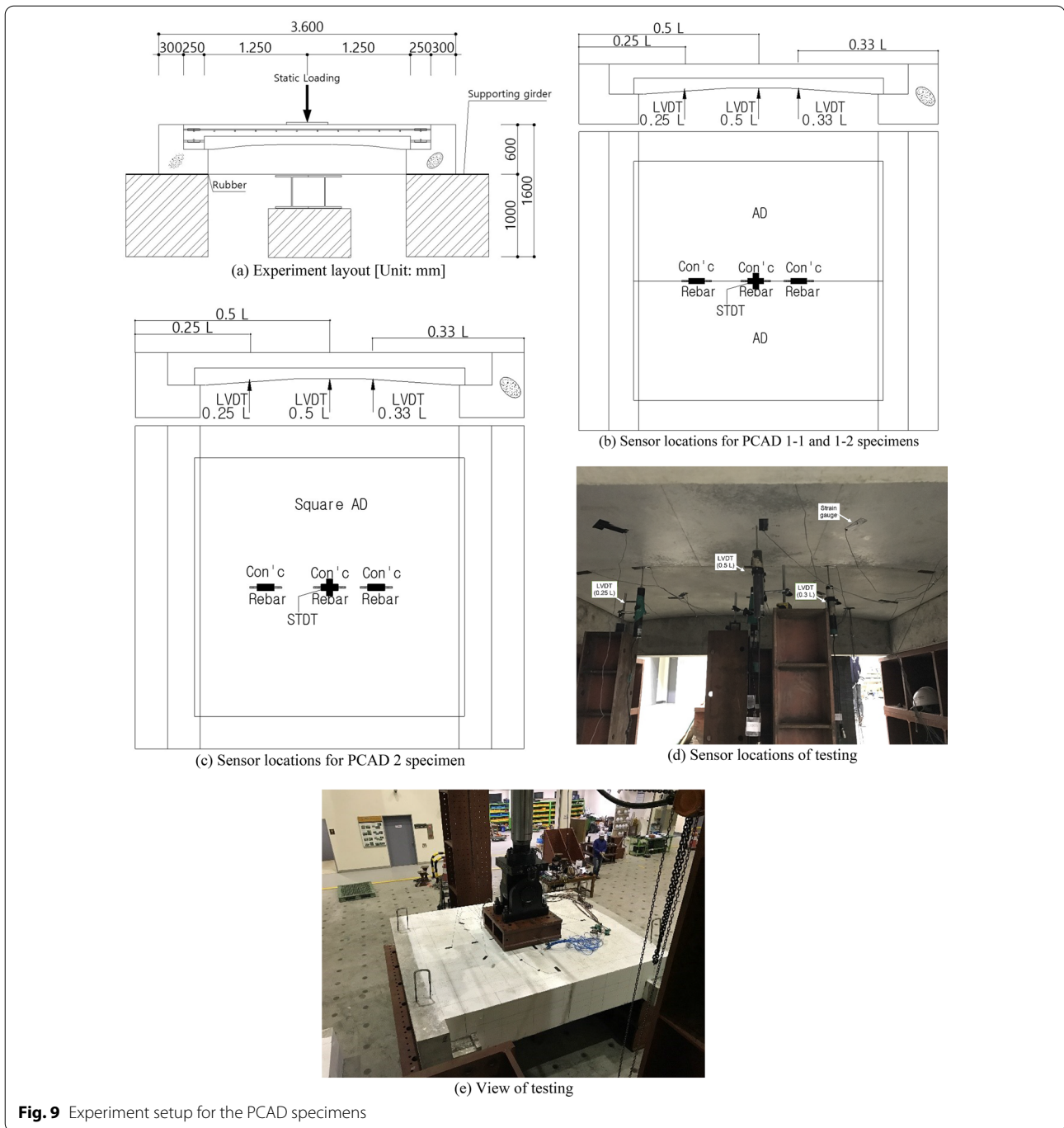


Fig. 9 Experiment setup for the PCAD specimens

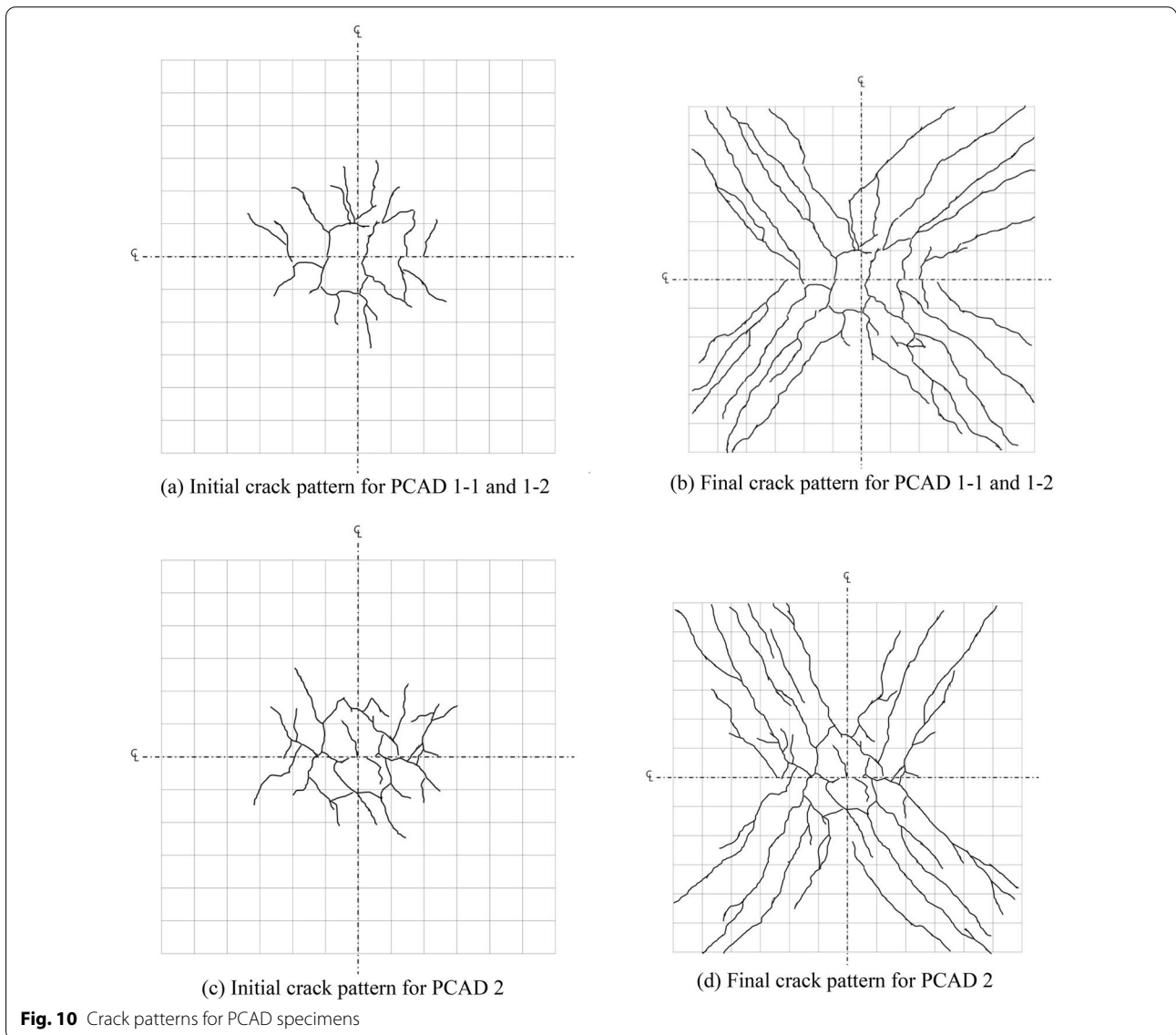
Table 3 Loading sequence for the specimens.

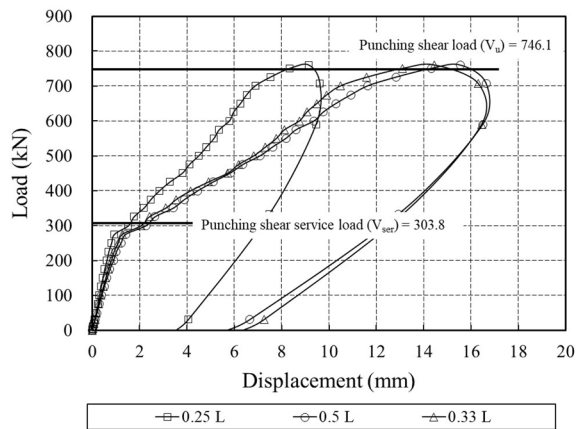
Loading sequence (kN)	Loading rate (mm/min)	Crack checking cycle (kN)
0–300	0.3	–
300–650	0.2	50
650– P_u	0.5	

and Collins (1986). Similar to the multidirectional fixed crack model, the total strain based crack models follow a smeared approach to calculate the fracture energy. The three-dimensional extension to this theory is proposed by Selby and Vecchio (1993). The smeared crack model is further divided into fixed crack and rotating crack model. The fixed crack model assumes that the crack axis does not change, once determined. This model can specifically

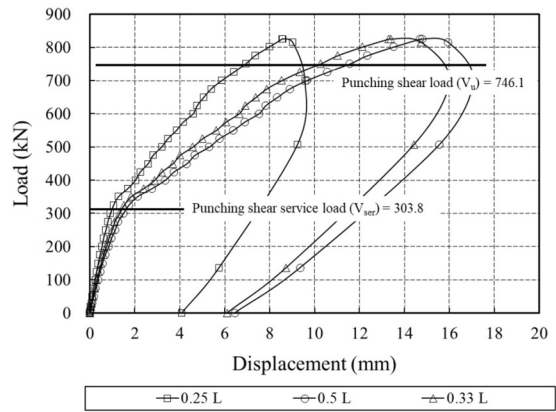
Table 4 Summary of the test results and design parameters for the specimens (Unit: kN).

Load		PCAD 1-1	PCAD 1-2	PCAD 1 _{aver}	PCAD 2
Test	Cracking load ($P_{cr,p,test}$)	300.0	350.0	325.0	350.0
	Yield load ($P_{y,p,test}$)	625.3	675.2	650.3	675.2
	Ultimate load ($P_{u,p,test}$)	759.8	825.0	792.4	819.5
KHBD	Design punching shear service load ($V_{ser,khbd}$)	303.8			
	Design punching shear strength ($V_{u,khbd}$)	746.1			
ACI 318	Design punching shear strength ($V_{u,aci}$)	750.4			
Eurocode 2	Design punching shear strength ($V_{u,ec2}$)	724.5			
Failure mode		Punching shear failure			

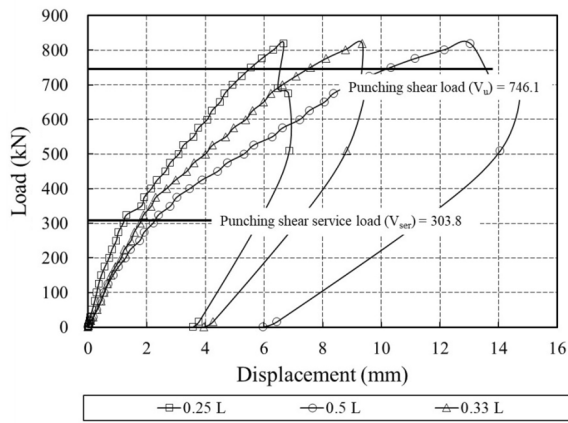




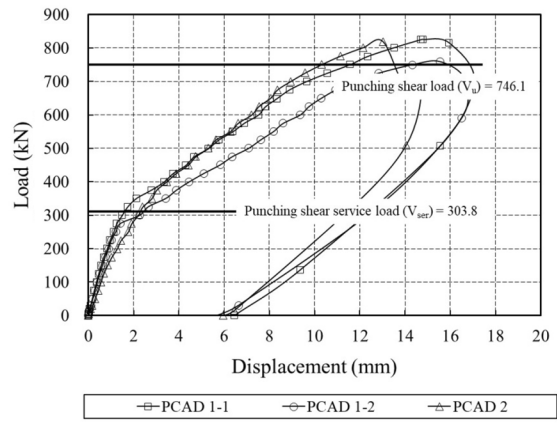
(a) Load-displacement relationship for PCAD 1-1 specimen



(b) Load-displacement relationship for PCAD 1-2 specimen



(c) Load-displacement relationship for PCAD 2 specimen



(d) Load-displacement relationship at mid-span for all specimens

Fig. 11 Load–displacement relationship for PCAD specimens

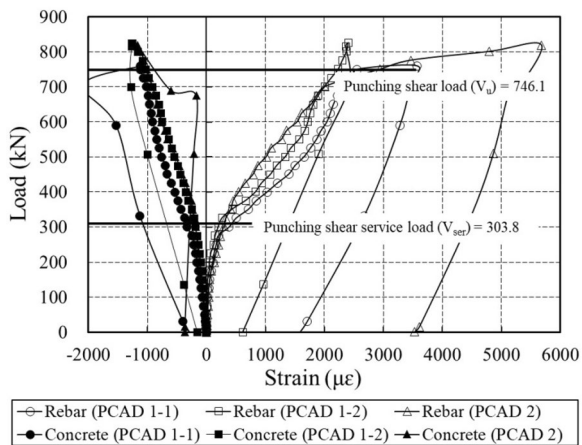


Fig. 12 Load–strain relationship for PCAD specimens.

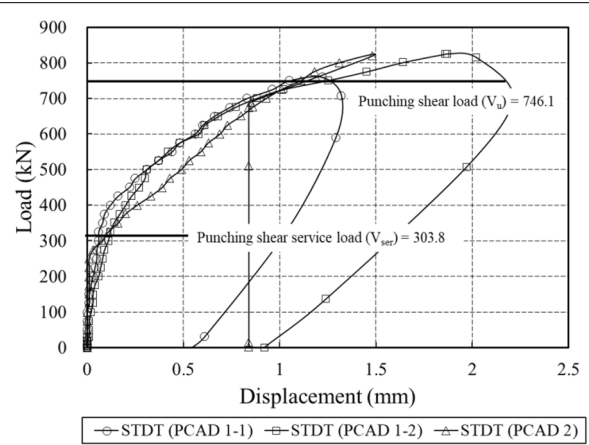


Fig. 13 Joint behavior for PCAD specimens.

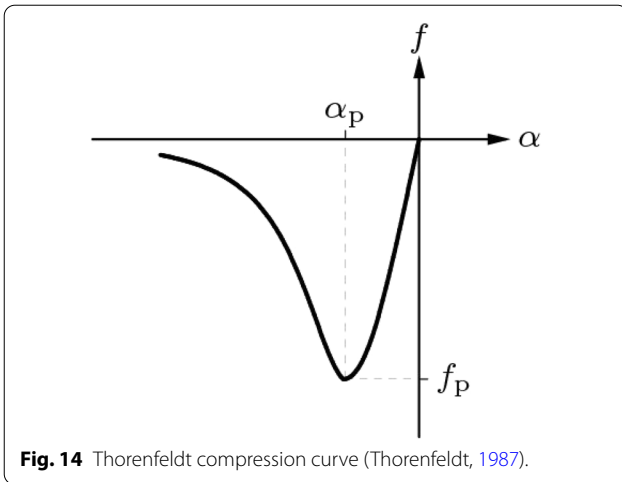


Fig. 14 Thorenfeldt compression curve (Thorenfeldt, 1987).

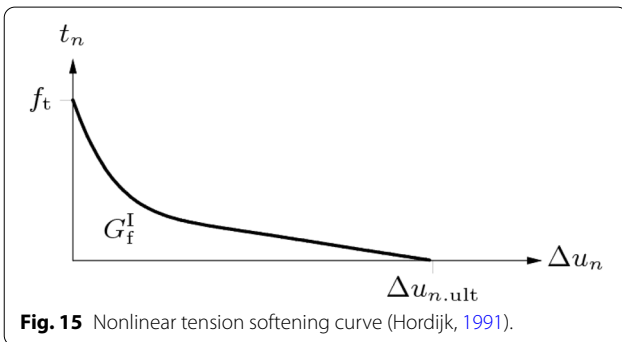


Fig. 15 Nonlinear tension softening curve (Hordijk, 1991).

apply the physical properties of cracks, but tends to slightly overestimate for stiffness and strength. On the other hand, the algorithm of the rotating crack model is relatively simple and easily converging compared to the fixed crack model due to crack axis being controlled by the strain.

The rotating crack model implemented in MIDAS FEA was used in this FE simulation. A brief description of the constitutive modeling of concrete is presented herein. The model includes two major failure mechanisms of concrete with regard to the tensile cracking and the compressive crushing. Thorenfeldt parabola was used for describing the compressive behavior of concrete, as shown in Fig. 14 (Thorenfeldt,

1987). Thorenfeldt function is described in the following equation:

$$f = -f_p \frac{\alpha_i}{\alpha_p} \left(\frac{n}{n-1 + \left(\frac{\alpha_i}{\alpha_p}\right)^{nk}} \right) \tag{7}$$

where $n = 0.80 + \frac{f_{iu}}{17}$, $k = \begin{cases} 1, & \text{if } 0 > \alpha > \alpha_p \\ 0.67 + \frac{f_{iu}}{62}, & \text{if } \alpha \leq \alpha_0 \end{cases}$

Tension limit in concrete is defined by a stress-fracture energy approach as proposed by Hordijk (1991), as shown in Fig. 15. This model assumes that softening phenomena occurs when the tensile strength is exceeded, and the slope of softening is determined by the fracture energy (G_f^I) and mesh size (h) parameters. The fracture energy G_f^I is obtained from the CEB-FIP code (1991), and the value of the fracture energy for each member differs depending on the compressive strength of concrete and the coarse aggregate size. The aggregate maximum size was 25 mm for all concrete and the mesh size was selected as 50 mm for all specimens. The model is given by the following equation:

$$\frac{\sigma_{nn}^{cr}(\epsilon_{nn}^{cr})}{f_t} = \begin{cases} \left[1 + \left(c_1 \frac{\epsilon_{nn}^{cr}}{\epsilon_{nn,ult}^{cr}} \right)^3 \right] \exp\left(-c_2 \frac{\epsilon_{nn}^{cr}}{\epsilon_{nn,ult}^{cr}}\right) \dots \\ -\frac{\epsilon_{nn}^{cr}}{\epsilon_{nn,ult}^{cr}} (1 + c_1^3) \exp(-c_2), & \text{if } 0 < \epsilon_{nn}^{cr} < \epsilon_{nn,ult}^{cr} \\ 0, & \text{if } \epsilon_{nn,ult}^{cr} < \epsilon_{nn}^{cr} < 0 \end{cases} \tag{8}$$

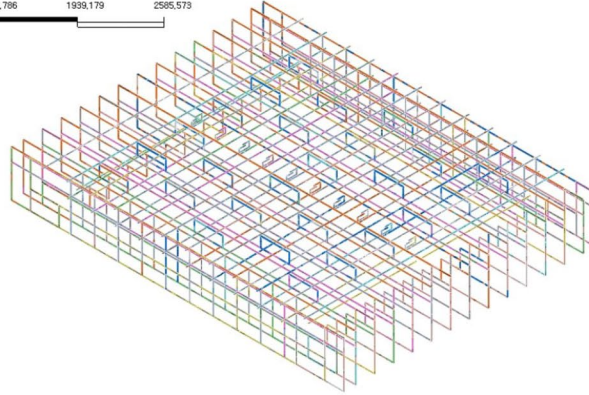
where $c1 = 3$ and $c2 = 6.93$.

von Mises plasticity function was used to model yielding of embedded rebars for nonlinear behavior. The elastic behavior of rebar is defined by specifying the Poisson’s ratio (ν) and Young’s modulus (E_s). The material properties of concrete and rebar for PCAD specimen are tabulated in Table 5.

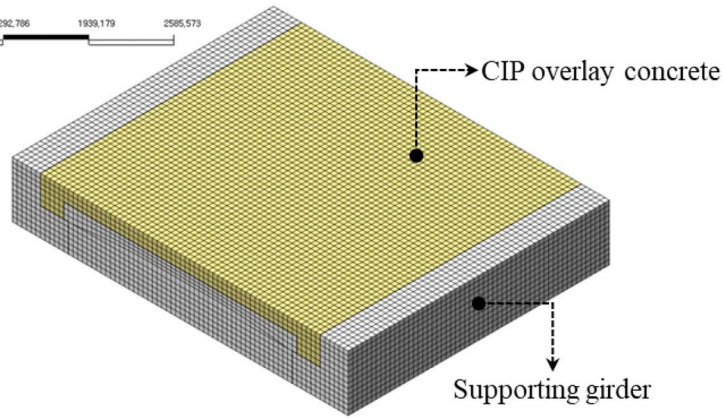
A three-dimensional simulation was conducted for the two specimens (PCAD 1 and 2) using 8-node isoparametric element and embedded bar element for concrete and rebar, respectively. BCs of all specimen were vertically and laterally restrained at contact surface nodes between supporting frames and girders, as same as the experimental conditions. The calibrated FE model was used without any further changes for the test specimens.

Table 5 Material models, criteria, and input parameters in FE simulations.

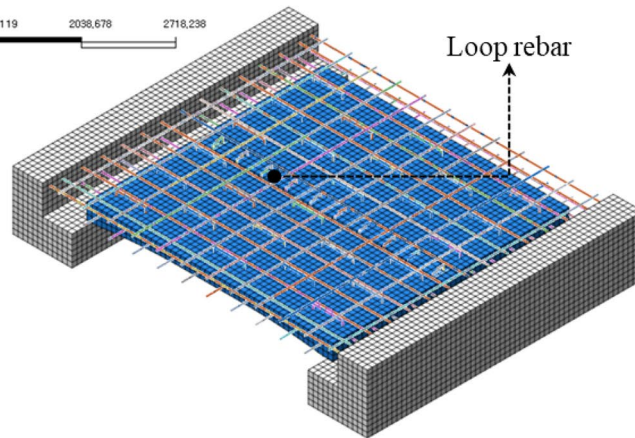
Material	Models/criteria	Young’s modulus (MPa)	Weight density (kN/m ³)	Poisson’s ratio	Strength (MPa)
Concrete	Hordijk (Tension model) Thorenfeldt (Compression model)	30,000	24.5	0.167	AD: 49.5 CIP: 38.5
Rebar	von Mises (Yield criterion)	200,000	78.6	0.3	400



(a) Rebar modeling for PCAD specimen

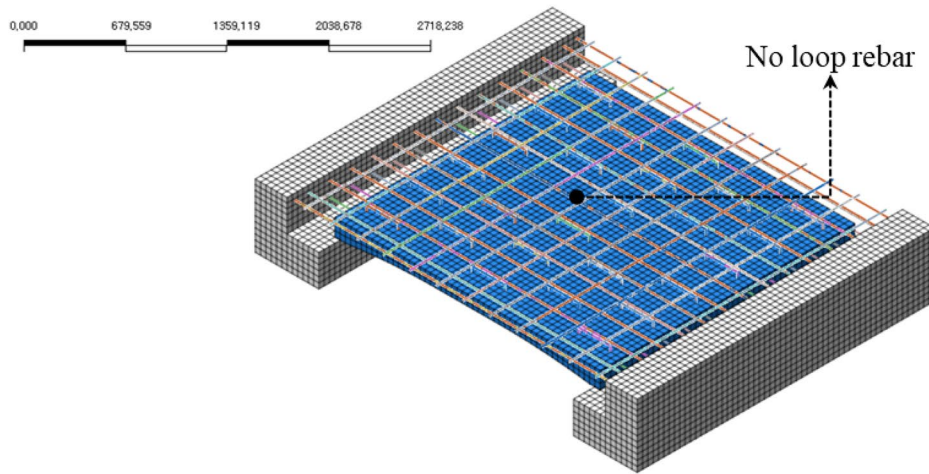


(b) Concrete modeling for PCAD specimen

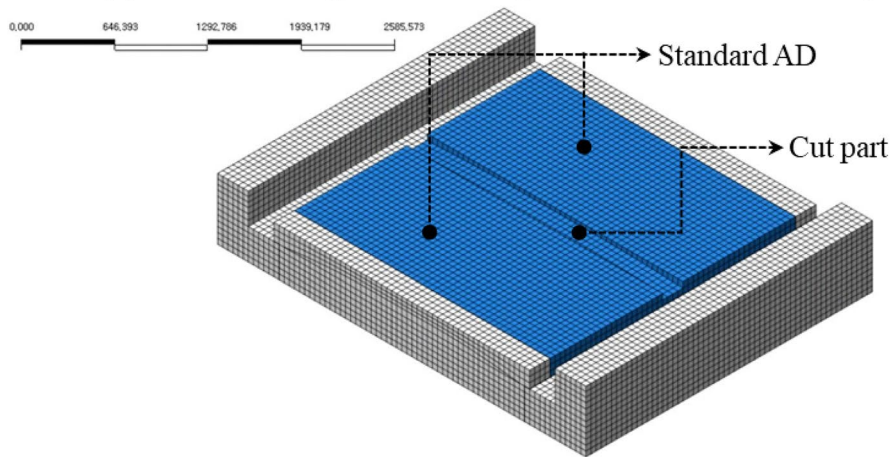


(c) Rebar modeling for PCAD 1 without CIP overlay concrete

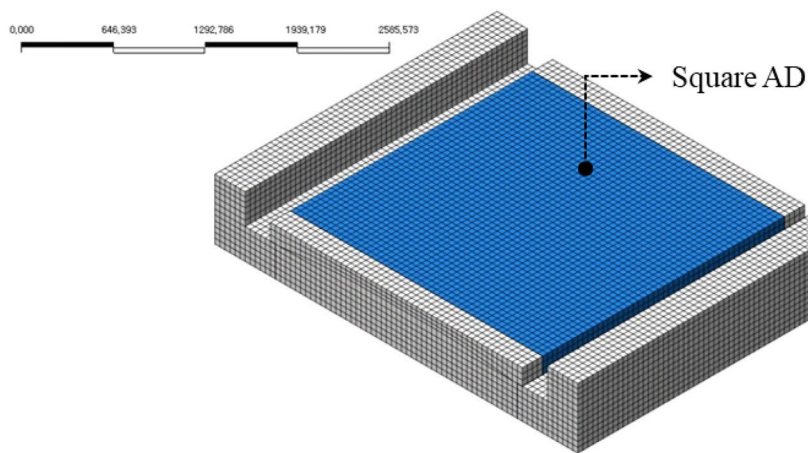
Fig. 16 FE modeling of PCAD specimens



(d) Rebar modeling for PCAD 2 specimen without CIP overlay concrete



(e) Concrete modeling for PCAD 1 specimen without CIP overlay concrete



(f) Concrete modeling for PCAD 2 specimen without CIP overlay concrete

Fig. 16 continued

The PCAD 1 and 2, consisting of rebar and concrete, were modeled, as shown in Figs. 15f and 16a with different colors used to distinguish the supporting girder concrete element, CIP concrete overlay element, and AD concrete element. PCAD 1 consisted of two standard ADs, and PCAD 2 consisted of one square AD. The difference of the PCAD 1 and 2 is that the PCAD 1 is the precast member which is connected by top loop rebars, poured with CIP overlay concrete, whereas PCAD 2 is a continued single casted precast member without loop rebar. The detailed joint modeling of PCAD 1 is shown in Figs. 4c, 16c, and e. In the FE model, PCAD 1 is modeled with connected nodes for both left and right members above the neutral axis and separated nodes between left and right member below the neutral axis for discontinuous behavior. The FE method for simulating the behavior of AD and girder is the same as the experiment process. An elastic link was applied to the interface between concrete elements and rubber element, and friction coefficient of 0.4 was taken in Caltrans (1994). Dowel bars of AD and the supporting girder interface were modeled as rigid links. Interfaces of each concrete element (precast AD, CIP, and girder) were also applied as rigid links. At the symmetric axis of AD, the nodes were tied to the lateral and only vertical displacement was allowed. In addition, MIDAS FEA supports the construction stage analysis function, and in this study, lateral restraints of AD and casting of CIP overlay concrete can be implemented in each stage. The boundary condition and concrete material model for PCAD 1 and 2 are same except the interface node condition.

6.2 Validation of the FEA Results for Deflection

The experiment and FEA results for each specimen are presented in Fig. 17 and Table 5. In the numerical

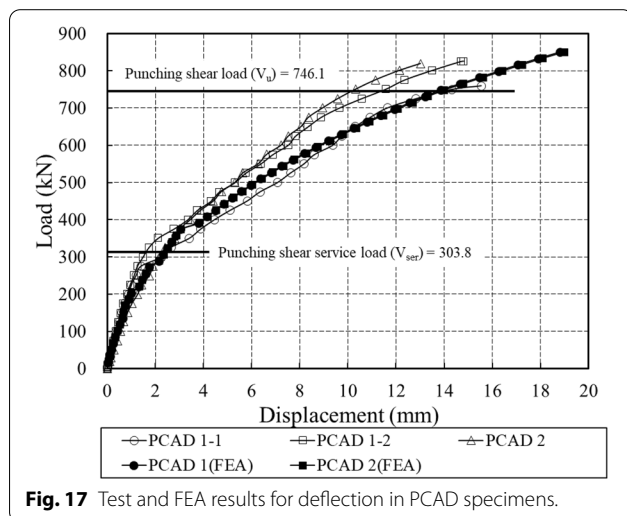


Fig. 17 Test and FEA results for deflection in PCAD specimens.

simulation, the difference in deflection between PCAD 1 and 2 is 1%, which come from the joint connection condition. PCAD 1 was slightly better, since PCAD 1 has additional loop rebar which is connected, but PCAD 2 has no loop rebar. Concrete is not a completely homogeneous material, so there are inherent differences in the test specimens. On the other hand, FEA considers concrete as a homogeneous material, so that there would be a slight difference in the results from the simulations to the tests. In addition, the contact area of AD is actually very small, and there will no significant difference just by disconnection of this part of the node. Overall, based on a comprehensive simulations of the test specimen, the punching shear capacity of PCADs 1 and 2 can be considered to be same.

As shown in Fig. 17, the load–displacement curve obtained from the FEA at mid-span exhibited bi-linear behavior, which was similar to the experiment results. The initial stiffness corresponded very closely to the measured data, but after approximately 370 kN, the stiffness was slightly lower than that of PCAD 1–2 and 2. This is similar to the experimental results, where the stiffness declined due to cracking at approximately 370 kN. However, the differences were not significant. The ultimate load of the test was lower than the FEA results, because the applied loading was stopped in the test at approximately 800 kN to prevent catastrophic failure of the specimens for safety reasons. Therefore, it is expected that the PCAD specimens could resist higher loads, because there was no significant decrease in stiffness.

6.3 Validation of the FEA Results for Strain

As shown in Fig. 18, the relationship between the load and the rebar strain in PCADs 1 and 2 were exactly the same as for the load–displacement relationship. The

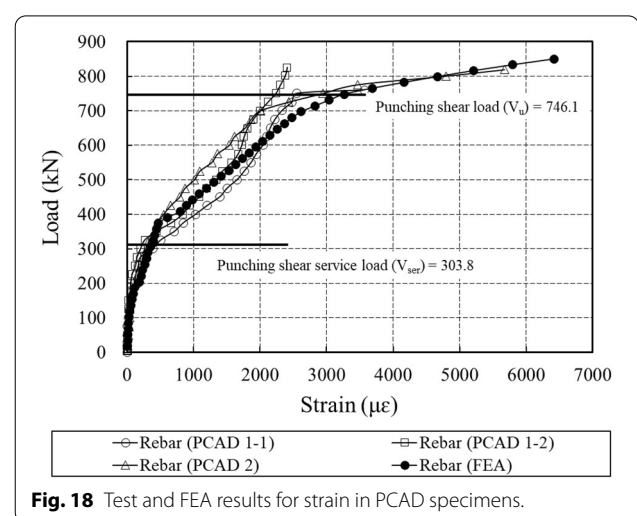
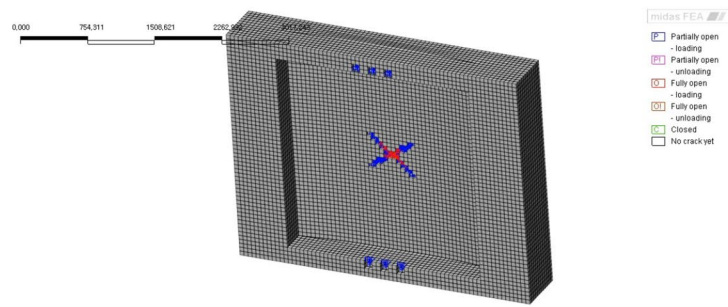
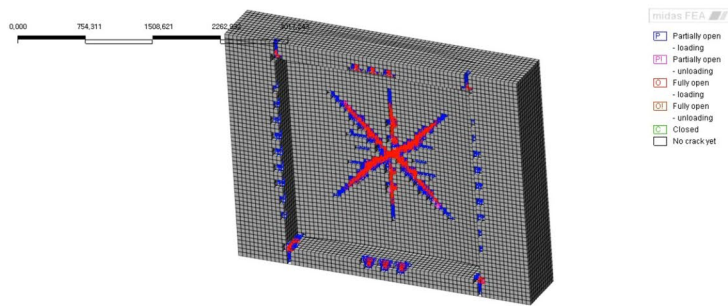


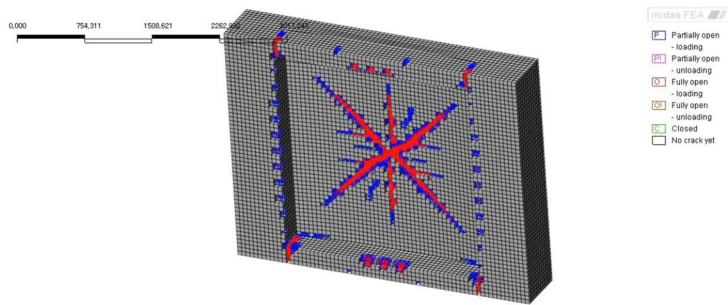
Fig. 18 Test and FEA results for strain in PCAD specimens.



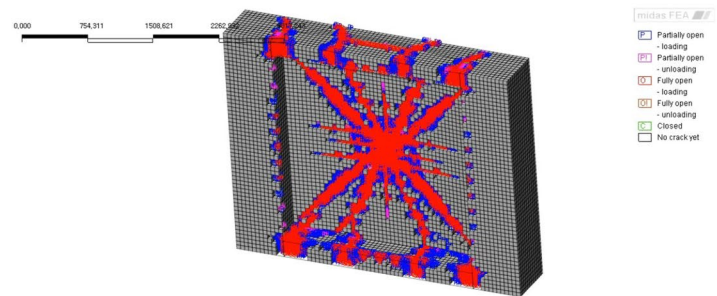
(a) Crack propagation at 374 kN



(b) Crack propagation at 500 kN



(c) Crack propagation at 650 kN



(d) Crack propagation at P_u

Fig. 19 Test and FEA results for failure mode in PCAD specimens

overall trend in the FEA results was similar to those from the experiment, with the rebar strain also exhibiting bi-linear behavior. At approximately 700 kN, the strain reached 2800 $\mu\epsilon$ and strain hardening behavior was observed; the simulation result showed the structure have reached a state of yielding.

6.4 Validation of the FEA Results for Failure Mode

Fig. 19a–d illustrates the crack pattern at the bottom surface from the initial cracking load to the ultimate load as observed from the experiment and the FE simulation. The cracking propagation process in the FE simulation results followed the four loading steps. At 374 kN, the cracking was concentrated around the center as radial cracks (Fig. 19a). By 500 kN, the radial cracks had developed and propagated, and flexural cracks were newly formed in the longitudinal direction (Fig. 19b). At this stage, radial and flexural cracks became significantly visible. At 650 kN, the radial and flexural cracks grew further, and some lateral cracks appeared for the first time (Fig. 19c). Finally, at the ultimate load, punching shear cracks formed suddenly around the loading location (Fig. 19d). At this stage, concrete crushing cracks formed around the loading plate, and the front and rear faces of the PCAD were destroyed by diagonal and flexural cracks. The TSC model based on fracture energy is implemented in the simulation, as smeared crack models (MIDAS, 2012 and DIANA, 2012). As shown in Figs. 10a–d and 19a–d, all crack patterns acquired from the FE simulation were similar to the cracking patterns observed from the experiments.

7 Prediction for Punching Shear Behavior Using Analytical Approach

The previous section indirectly verified that the structural performance of the proposed AD was superior to that of the FD by comparing the various study results. However, this has not been directly verified with the FD. Therefore, in the arching action verification section, the behavior of each deck (AD and FD) according to various design factor in the static load testing, and the punching shear testing is analyzed using a calibrated FE model.

The structural performance of SSAD and SSFD, which are without CIP overlay concrete was compared to verify the arching action of the deck directly. Two FE models are additionally considered: a model which is laterally restrained (LR) and a model in which the laterally unrestrained (LU) in AD and FD, as shown in Fig. 20a–c. The FD was additionally analyzed for thicknesses of both 100 and 160 mm due to the central and end thicknesses of the arch deck were 100 and 160 mm, respectively. The basic simulation conditions for the AD and FD, and all of the other material properties and BCs for the supporting

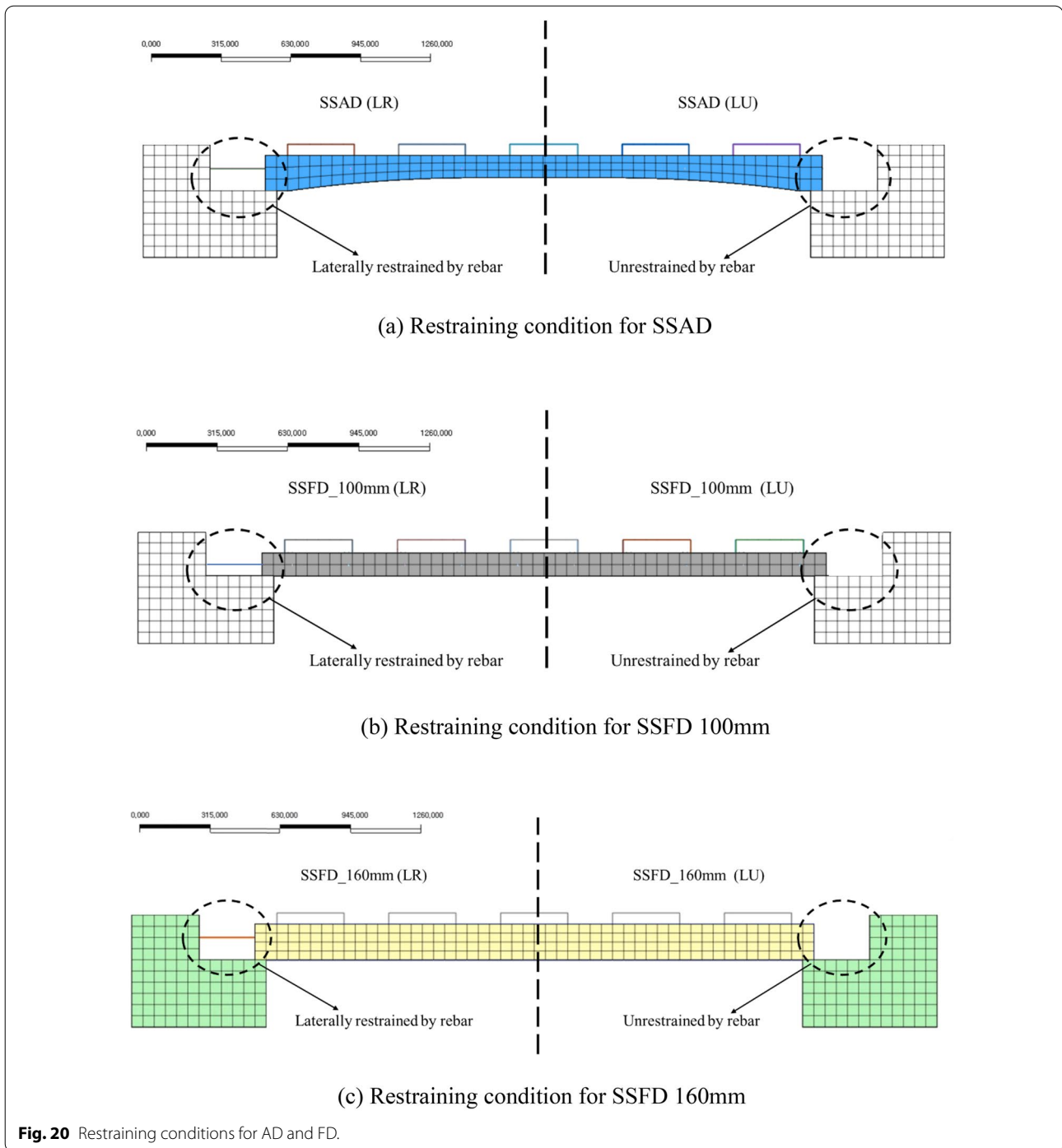
girder were the same. Based on the above results, the focus of this study is still PCAD 1, which consist of standard ADs. Therefore, analytical studies such as arching action and parametric verification were performed using the standard AD model.

7.1 Arching Action Verification of the SSAD and SSFD

The load–displacement relationship for an SSAD and SSFD are presented in Fig. 21. The lowest stiffness was observed for the 100 mm FD (LU) and the 160 mm FD (LR) had the highest initial stiffness of the analyzed models, but at approximately 50 kN, greater deflection occurred in the FD than in the AD, meaning that the stiffness of the AD was higher than that of the 160 mm FD at this point, due to the difference between the arching action from structural shape in the AD and FD. The investigation of the difference between the LR and LU models, AD, 160 mm FD, and 100 mm FD showed deflection of approximately 15%, 3–5%, and 7–10%, respectively, in which the LR model showed better structural performance than the LU model. In particular, AD was found to be greatly affected by both the arching action from the structural shape and the lateral constraint. However, the initial cracking load of 160 mm FD was observed at 10–15 kN, whereas both cracking load of AD and 100 mm FD occurred at 8 kN. It was found that the cracks were significantly affected by the thickness of the deck rather than the arching action. In addition, an AD that is laterally constrained by transverse rebar had a similar load-carrying capacity than 160 mm FD, even though the center of the AD was 100 mm thick. These results verified that laterally restrained ADs are structurally more effective in resisting applied load.

7.2 Arching Action Verification of the PCAD and PCFD

The load–displacement relationship for the PCAD and PCFD are shown in Fig. 22. The FE simulation results for the composite decks were different from the FE simulation results for the single decks. The 100 mm FD had the lowest cracking load and load-carrying capacity as expected, but the load–displacement relationship for the AD and the 160 mm FD was very similar. The 100 mm FD had the lowest cracking load at 290 kN, and the AD and 160 mm FD had a similar initial stiffness up to a load of approximately 550 kN, but above 550 kN, the stiffness of the 160 mm FD was slightly higher. A single FD did not have a high load-carrying capacity, since it was laterally unrestrained by rebar, but the composite FD has a CIP concrete overlay on the top, which constrained the lateral strain. Therefore, in an actual bridge, if the deck is mounted on a girder and a CIP overlay concrete is casted, it will have the similar laterally restraining effect as the rebar.



Nevertheless, it is important to note that the AD has a central thickness of 100 mm, and it has a similar stiffness to the 160 mm FD, illustrating the structural advantage that derives from the arch shape. As stated earlier, an AD has one form of arching action that occurs under lateral restraint from rebar and another form that occurs due to the shape of the arch. Therefore, the arching actions that occur under these two conditions complement each other and lead to higher

structural load resisting capacity and stable failure behavior (Table 6).

7.3 Prediction Formula for Punching Shear Resistance of AD

The punching shear resistance of AD still follows in this paper with the conventional codes, such as KHBD, ACI

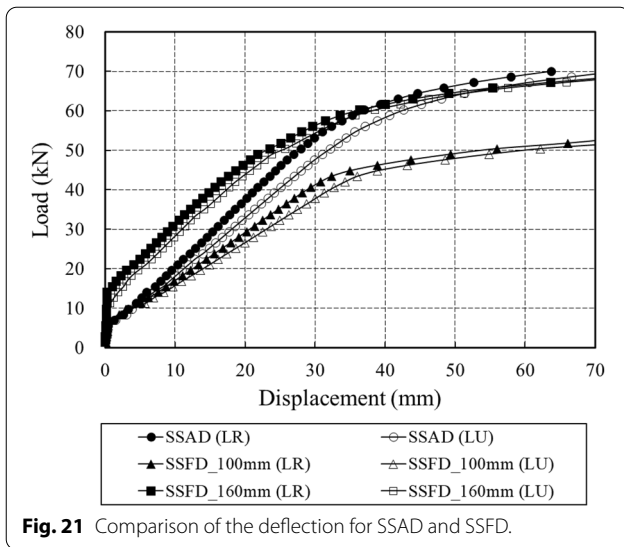


Fig. 21 Comparison of the deflection for SSAD and SSFD.

318 and Eurocode 2, as shown in Sects. 4 and 5. The calculated code results were slightly lower than the experimental results. It is more appropriate to predict the punching shear resistance of FD than AD due to the conventional codes do not consider the characteristic of the arching action. Therefore, a more accurate prediction formula should be developed for punching shear resistance of AD. In this study, the perimeter of critical section calculation formula by Huang et al. (2015) is applied for Eurocode 2 to predict the punching shear resistance performance of the AD. Specimens used in their study were a steel–concrete composite arch structure. Therefore, if the steel member is excluded from the composite structure to consider only the concrete core section, that the prediction formula can be applied to this study.

7.3.1 Modification for the Perimeter of Critical Section

Punching shear prediction by Eurocode 2 does not consider the effect of curvature, and proposes a constant perimeter of critical section with at a distance $2d$ from loading area. However, it has been experimentally proven that the change in curvature has a significant effect on punching shear load by Shukry and Goode (1990), Huang et al. (2015) and Yan et al. (2016). To develop an

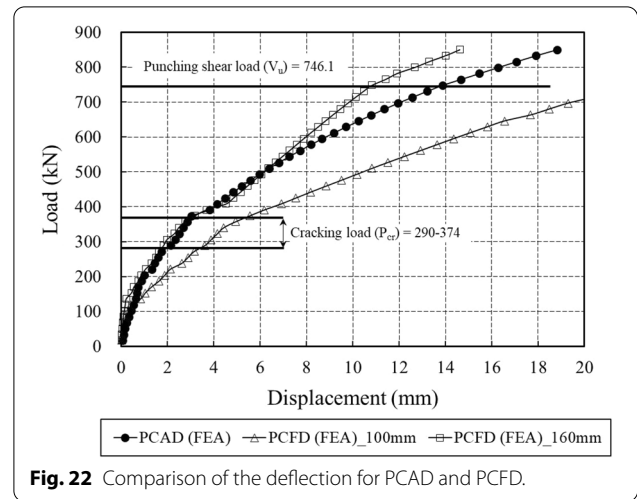


Fig. 22 Comparison of the deflection for PCAD and PCFD.

accurate prediction model of AD, it is necessary to modify the perimeter of critical section considering for the curvature.

The perimeter of critical section for AD is shown in Fig. 23a, b. Huang et al. (2015) assumed that the perimeter of critical section initiates at the reflection point [where the section moment $M_{arc}(x) = 0$] in the circumferential direction based on the fact that the angle of the punching shear plane is curvature-dependent theory. For calculating the crack angle followed the minimum value of 26.6° according to Eurocode 2. Hence, the perimeter of critical section u_1 can be followed by

$$u_1 = 2(L_a + L_b) \tag{9}$$

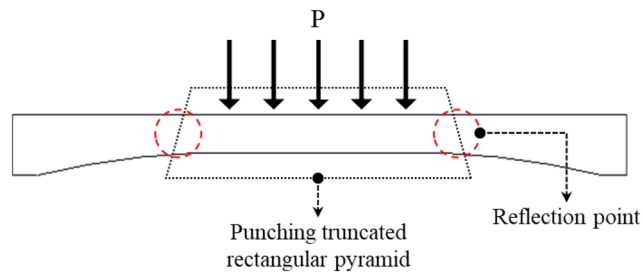
where $L_a = 2x$ which is obtained from making sectional bending moment $M_{arc}(x) = 0$, while L_b is obtained by $L_b = l_b + (2h_c / \tan\theta_{wid})$.

According to Huang et al. (2015), the calculation for internal force of fixed end arch is as follows and can be refer to Fig. 23c, d.

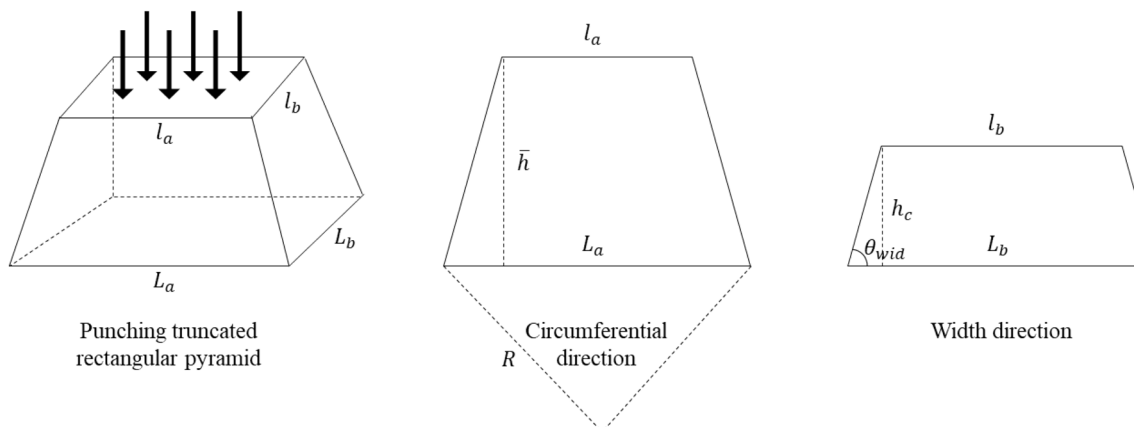
- (1) Choose an equivalent model with a rigid arm element ($EI = \infty$);
- (2) Cut the rigid arm element and establish the compatibility equations at point C;

Table 6 Comparison of test and FE simulation results with various parameters.

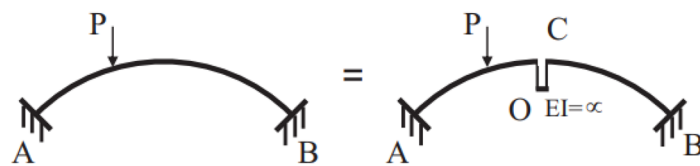
Specimens	P_u (kN)	$V_{u,khbd}$ (kN)	$V_{u,aci}$ (kN)	$V_{u,ec2}$ (kN)	P_{cr} (kN)	$V_{ser,khbd}$ (kN)	ΔP_u (mm)	ΔV_{ser} (mm)	ΔV_u (mm)	$\Delta V_{u,test} / \Delta V_{u,FEA}$
PCAD 1-1	759.8	746.1	750.4	724.5	300	303.8	15.5	2.2	6.4	1.14
PCAD 1-2	825.0				350		14.8	1.5	4.7	0.84
PCAD 1 _{aver}	792.4				325		15.2	1.9	5.6	1.00
PCAD 2	819.5				350		13.0	2.2	4.8	0.86
PCAD FEA	850	–			374	–	18.8	2.3	5.6	–



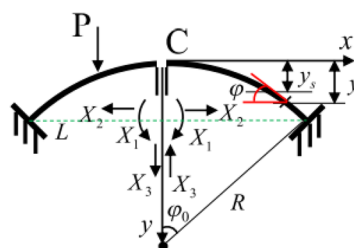
(a) Concept of the perimeter of critical section in AD under punching shear load



(b) Punched concrete truncated rectangular pyramid (Huang et al. (2015))



(c) Equivalent model for fixed end arch (Huang et al. (2015))



(d) Basic determined model subject to forces X_1, X_2, X_3 (Huang et al. (2015))

Fig. 23 Perimeter of critical section for AD.

Table 7 Calculated punching shear strengths by the proposed formula.

Parameters	Rebar ratio (%)					Concrete strength (MPa)				
	60	80	AD (100)	120	140	30	40	AD (50)	60	70
Design factor	60	80	AD (100)	120	140	30	40	AD (50)	60	70
Punching shear strength ($V_{u,pro}$, kN)	720.5	768.4	808.8	844.2	875.8	720.5	768.4	808.8	844.2	875.8

$$y = R \cos \varphi, x = R \sin \varphi, ds = R d\varphi, \sin \varphi_0 = \frac{L}{2R}, y_s = \int \frac{y}{EI} ds / \int \frac{1}{EI} ds \tag{10}$$

$$\begin{cases} \delta_{11}X_1 + \Delta_{1P} = 0 \\ \delta_{22}X_2 + \Delta_{2P} = 0 \\ \delta_{33}X_3 + \Delta_{3P} = 0 \end{cases} \tag{11}$$

where

$$\begin{aligned} \delta_{11} &= \int \frac{\overline{M}_1^2}{EI} ds = \int \frac{1}{EI} ds, \\ \delta_{22} &= \int \frac{\overline{M}_1^2}{EI} ds + \int \frac{F_{N2}^2}{EI} ds \\ &= \int \frac{(y - y_s)^2}{EI} ds + \int \frac{\cos^2 \varphi}{EI} ds, \\ \delta_{33} &= \int \frac{\overline{M}_3^2}{EI} ds = \int \frac{x^2}{EI} ds; \\ \Delta_{1P} &= \int \frac{\overline{M}_1 M_P}{EI} ds, \\ \Delta_{2P} &= \int \frac{\overline{M}_2 M_P}{EI} ds, \Delta_{3P} = \int \frac{\overline{M}_3 M_P}{EI} ds \end{aligned} \tag{12}$$

where M_P is the bending moment in a basic determined structure subject to outer force P ;

For arch member subject to uniform load, $M_P = -(q/2)x^2$;

For arch member subject to point load, $M_P = -(\frac{P}{2})x$;

For arch member subject to patch load, $M_P = -(\frac{qc^2}{2}) - qcx$;

(3) Solve $X_1X_2X_3$ and substitute them to the internal force equation resulting in

$$M = X_1 + X_2(y - y_s) + X_3x + M_P \tag{13}$$

$$F_Q = X_2 \sin \varphi + X_3 \cos \varphi + F_{QP} \tag{14}$$

$$F_N = -X_2 \cos \varphi + X_3 \sin \varphi + F_{NP} \tag{15}$$

Let $M|x = 0$, the position of inflection point x can be solved.

7.4 Parametric Analysis of the PCAD

Parametric study of transverse rebar ratio and concrete strength on standard AD are perform to investigate the behavior of PCAD 1 for comparison to various design factors. The rebar ratio and concrete strength of 60, 80, 120, and 140% for tested specimens, respectively, are

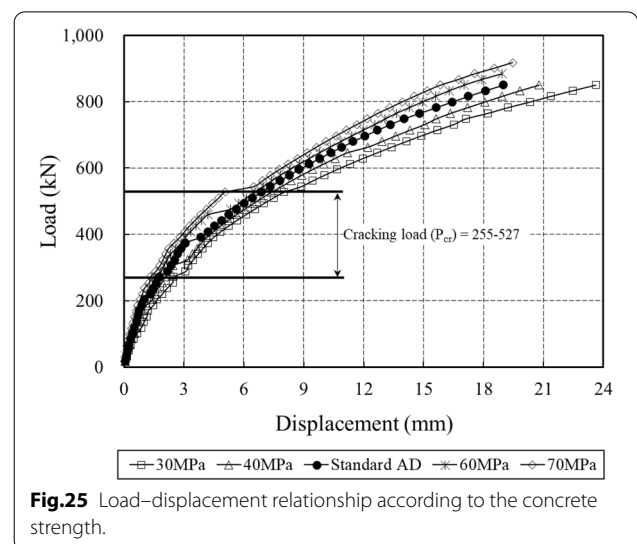
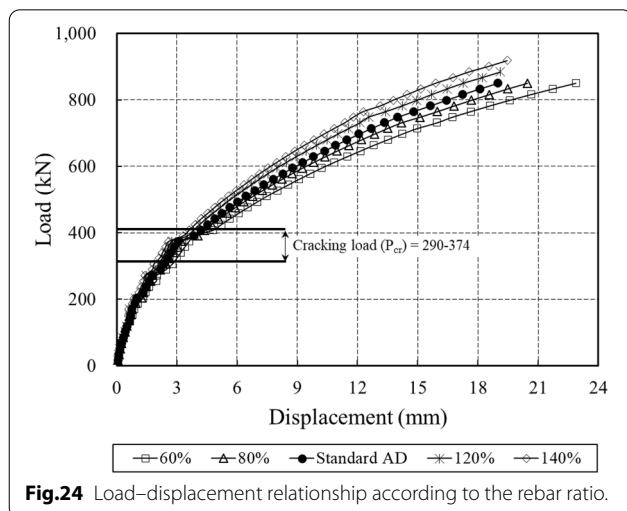


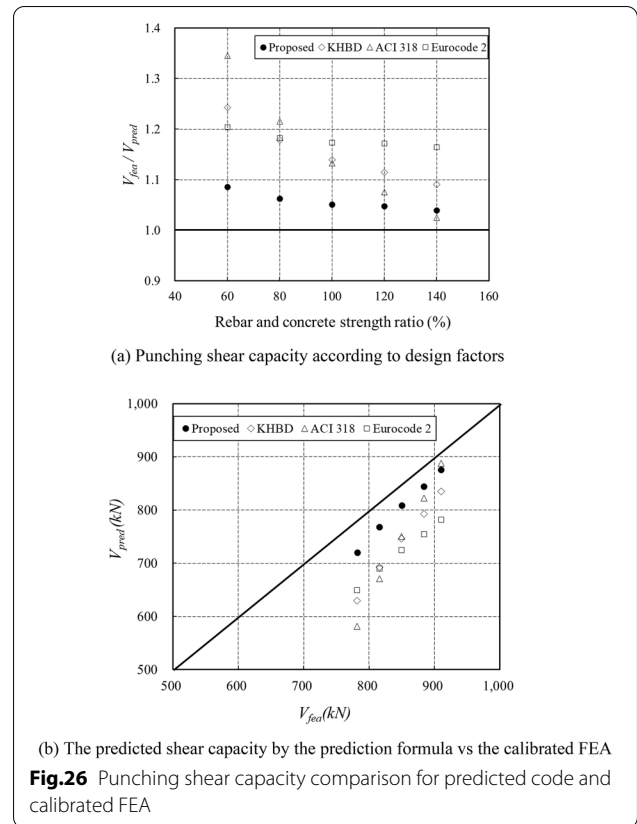
Fig.24 Load-displacement relationship according to the rebar ratio.

Fig.25 Load-displacement relationship according to the concrete strength.

used in the parametric FE models. The punching shear strengths for various parametric values obtained from the simulations and the equation proposed in this study based on the Eurocode 2 equation are compared. The punching shear strength obtained in FEA is when the maximum deflection reaches 20 mm, which is the same as the maximum deflection of the test specimen, and this is the span length (L) of AD divided by 125 ($\delta_{limit} = L/125$). The same boundary conditions and material models are used for the parametric study simulations as that of the calibrated PCAD 1 model. The calculated punching shear strengths by the proposed formula is tabulated in Table 7.

The results of the load–displacement relationship for PCAD 1 from the rebar ratio variation are presented in Fig. 24. The overall behavior history for all of the specimens showed bi-linear behavior with the cracking load of 374 kN for all of specimens. After the cracking load, non-linear behavior with varying slope for various rebar ratio occurred. The maximum deflection at 850 kN for the rebar ratio from 60, 80, 120, and 140% was approximately 22.88, 20.45, 17.27, and 15.89 mm, respectively, which are equivalent to approximately 120, 107, 91, and 84% of the maximum deflection of the test result of PCAD 1. The parametric study results for the transverse rebar ratio variation seems to be reasonable, since the increase in the ratio decreases the deflection accordingly.

The results of the load–displacement relationship for the concrete strength are shown in Fig. 25. The analysis results according to the concrete strength variation gave significantly different cracking load results compared to the rebar ratio variation. The cracking loads of each model from 30, 40, 60, and 70 MPa were 255, 306, 459, and 527 kN, respectively. However, the maximum deflections for various concrete strengths were similar. The concrete strength parametric study results seem to be also reasonable, since the deflection of the decks is controlled by the reinforcement ratio rather than concrete strength. The parametric study summary is that the maximum deflection of the decks is significantly affected by the transverse rebar ratio and the crack



load of the decks is significantly affected by concrete strength.

7.5 Punching Shear Capacity Comparison for Predicted Code and Calibrated FEA

In this study, the number of specimens was very limited. Therefore, the calibrated FEA model was assumed to be the experimental results and compared with the prediction code. As shown in Fig. 26a, b, although the punching shear strength calculated by proposed formula still conservatively predicted, it was confirmed to evaluate the strength relatively accurately compared to other

Table 8 Comparison of the punching shear capacity by proposed formula and current codes.

Model	Predicted strength (kN)					Strength ratio, $V_{u,fea}/V_{u,pred}$			
	$V_{u,fea}$	$V_{u,pro}$	$V_{u,khbd}$	$V_{u,aci}$	$V_{u,ec2}$	$V_{u,fea}/V_{u,pro}$	$V_{u,fea}/V_{u,khbd}$	$V_{u,fea}/V_{u,aci}$	$V_{u,fea}/V_{u,ec2}$
60%	782.0	720.5	629.3	581.3	649.3	1.09	1.24	1.35	1.20
80%	816.0	768.4	692.7	671.2	690.1	1.06	1.18	1.22	1.18
Standard AD (100%)	850.0	808.8	746.1	750.5	724.5	1.05	1.14	1.13	1.17
120%	884.0	84.2	792.9	822.1	754.6	1.05	1.11	1.08	1.17
140%	910.0	875.8	834.7	888.0	781.5	1.04	1.09	1.02	1.16
Mean						1.06	1.15	1.16	1.18
Standard deviation						0.02	0.05	0.11	0.01

codes. In particular, the mean values of KHBD, ACI 318, and Eurocode 2 for $V_{u,fea}/V_{u,pred}$ were 1.15, 1.16, and 1.18, respectively, but the mean value of the proposed formula was most similar to the calibrated FEA results ($V_{u,fea}/V_{u,pred} = 1.06$), as shown in Table 8. Also, the standard deviation was 0.02, so there was no significant deviation according to each parameter.

8 Conclusions

This paper presents the study of experimental and simulation verification for a newly proposed precast RC arch deck (AD) composite specimen under punching shear load. A total of three specimens were manufactured and tested to failure. Two PCAD 1 (1–1 and 1–2) specimens were manufactured with two standard ADs for each specimen, and one PCAD 2 was manufactured with a square AD. The specimens were tested under concentrated load on the center of the specimen. FE simulations were performed to validate the experimental results for punching shear strength for all of the specimen. In addition, the analytical studies were performed to confirm the arching action developed in AD, and to verify the proposed formula with calibrated FEA results. Based on the experimental and simulation results, the following conclusions can be drawn:

- (1) The average ultimate loads of PCAD 1 and 2 were 792.4 and 819.5 kN, respectively, which were approximately 1.06 and 1.1 times higher than the design punching shear load of 746.1 kN calculated from the design equations of the Korean Highway Bridge Design (KHBD) code, respectively. Also, the test results are greater than the design punching shear load of 483.3 and 469.5 as calculated from the equations of the ACI 318 and Eurocode 2, respectively.
- (2) The first cracks of PCAD 1–1, 1–2 and 2 occurred at 300, 350, and 350 kN, respectively, which were approximately 1.15–1.48 times higher than the design punching shear service load of 303.75 kN as calculated from the KHBD code. Radial cracks dominantly occurred due to arching action.
- (3) The maximum measured deflection at the design punching shear service load level (303.75 kN) was less than 2.3 mm, which is well below the allowable code limits. However, after 300 kN, large deflection and bi-linear behavior were observed due to concrete cracking.
- (4) Two FE models were considered to verify the arching action: a model in which the LR and a model in which the LU in AD and FD. The LR model showed better structural performance than the LU model. Especially, AD was found to be greatly affected by

both the arching action by the structural shape and the lateral constraint than FD. An AD that is laterally constrained by transverse rebar had a similar load-carrying capacity than 160 mm FD, even though the center of the AD was 100 mm thick. These results verified that laterally restrained ADs are structurally more effective in resisting applied load.

- (5) The parametric analyses were performed by selecting the transverse rebar and concrete strength ratio as 60, 80, 120, and 140% of the standard AD. The maximum deflection of the decks is significantly affected by the transverse rebar ratio and the crack load of the decks is significantly affected by concrete strength.
- (6) The proposed formula predicted the punching shear strength with a difference of approximately 6%, and the standard deviation was very small. The proposed formula in this study is more suitable than other codes for predicting the punching shear strength of AD.
- (7) Finally, a limitation of this study is that it cannot quantify the lateral constraint stiffness. To quantify the lateral constraint stiffness, experimental investigation and verification of additional parameters such as lateral displacement and rotation of end support is required. They should also be verified by appropriate analytical models. However, in this study, there is no way to quantify and represent the above parameters due to experimental verification of these parameters was not performed.

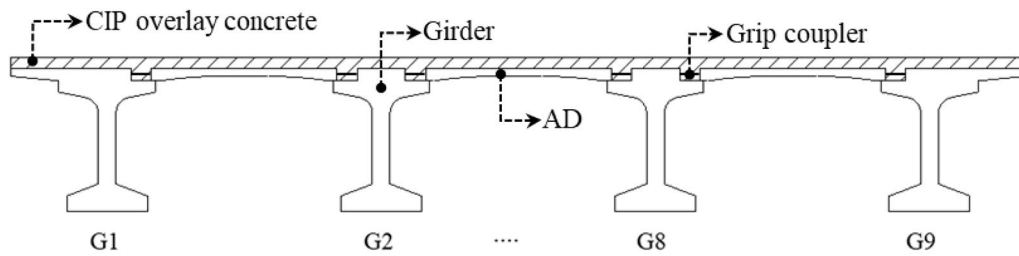
Appendix 1

Bridge Construction Method Using AD

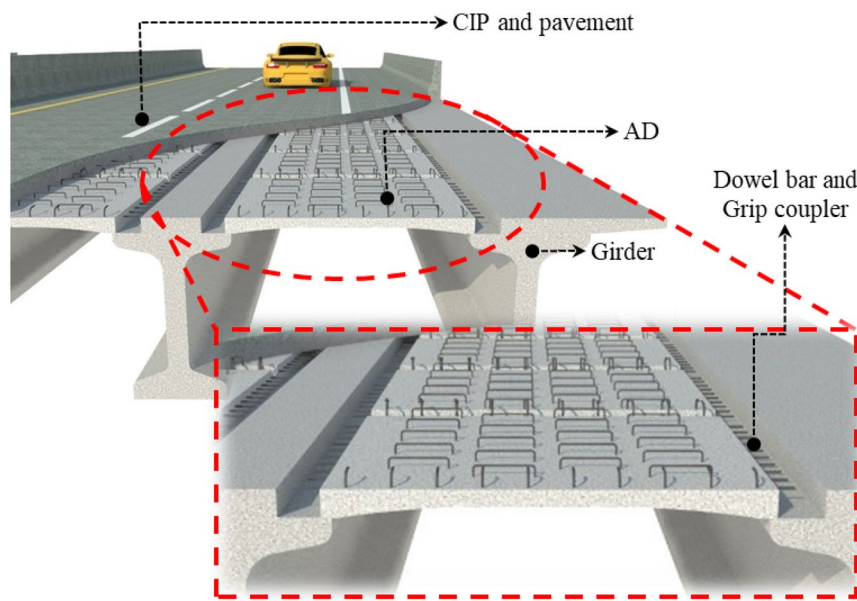
The newly proposed precast AD bridge is a composite structure of precast deck, girder members, and cast-in-place overlay concrete. The following descriptions were the bridge construction method using AD, and the detailed schematic is shown in Fig.

27.

- (1) Girder mounting: leave the spacing of girders as much as the lateral length of AD, but further narrow them by approximately 100–200 mm to mount AD on the upper flange of the girder.
- (2) Setup the grip coupler: insert the steel pipe sleeve coupler into the lateral dowel bar of the I-girder.
- (3) AD mounting on girder: mount AD and upper flange of girder so that each supporting point overlaps by 50–100 mm. (locate rubber pad at the con-



(a) Concrete girder bridge components using AD



(b) Schematic of Concrete girder bridge using AD

Fig. 27 Concrete Girder Bridge using AD. **a** Concrete girder bridge components using AD. **b** Schematic of Concrete girder bridge using AD.

tact area considering the factory manufacturing error and prevention of edge failure). Also, the AD and lateral dowel bars of the girder must be in line with each other to allow the steel pipe sleeve coupler to pass through.

- (4) Lateral restraint of AD: after mounting the steel pipe sleeve coupler between AD and the lateral dowel bar of the girder, press it with a grip press machine. This is a state in which the AD is laterally restrained by the dowel bar and the grip coupler, and the compressive force is introduced.
- (5) CIP casting and composition: CIP overlay concrete is casted into the empty space between AD and upper flange to complete the construction. (Please refer to Fig. 27).

Acknowledgements

This work is supported by the Korea Agency for Infrastructure Technology Advancement (KAIA) grant funded by the Ministry of Land, Infrastructure and Transport (Grant 21CFRP-C163382-01).

Author contributions

D-HY: a person who performed most of test and analysis works; a main writer of the paper. S-JC: a person who assisted the research and writing the paper. S-JK: a person who supported the research project and writing the paper. J-HJK: a PI of the research project, who planned and developed the main idea of the study. All authors read and approved the final manuscript.

Authors' information

Dal-Hun Yang, Researcher, Ph.D., Central Research Institute, Korea Hydro & Nuclear Power Co., Ltd., 70, Yuseong-daero 1312 beon-gil, Yuseong-gu, Daejeon, 34101, Republic of Korea.
 Seung-Jai Choi, Postdoctoral Researcher, Ph.D., School of Civil and Environmental Engineering, Yonsei University, 50, Yonsei-ro, Seodaemun-gu, Seoul, 03722, Republic of Korea.
 Sung-Jae Kim, CEO, Ph.D., Bridge Technology Co., Ltd., 520, Misa dae-ro, Hanam, Gyeonggi, Republic of Korea.
 Jang-Ho Jay Kim, Professor, Ph.D., School of Civil and Environmental Engineering, Yonsei University, 50, Yonsei-ro, Seodaemun-gu, Seoul, 03722, Republic of Korea.

Funding

Ministry of Land, Infrastructure and Transport (Grant 21CFRP-C163382-01).

Availability of Data and Materials

Not applicable.

Declarations**Ethics Approval and Consent to Participate**

Not applicable.

Consent for Publication

Not applicable.

Competing Interests

The authors declare that they have no competing interests.

Author details

¹Central Research Institute, Korea Hydro & Nuclear Power Co., Ltd., 70, Yuseong-daero 1312 beon-gil, Yuseong-gu, Daejeon 34101, Republic of Korea. ²School of Civil and Environmental Engineering, Yonsei University, 50, Yonsei-ro, Seodaemun-gu, Seoul 03722, Republic of Korea. ³Bridge Technology Co., Ltd., 520, Misa dae-ro, Hanam, Gyeonggi, Republic of Korea.

Received: 27 July 2021 Accepted: 1 July 2022

Published online: 21 November 2022

References

- Au, F. T. K., Wang, J. J., & Liu, G. D. (2003). Construction control of reinforced concrete arch bridges. *Journal of Bridge Engineering*, 8(1), 39–45.
- Amir, S., van der Veen, C., Walraven, J. C., & de Boer, A. (2016). Experiments on punching shear behavior of prestressed concrete bridge decks. *ACI Structural Journal*, 113(3), 627.
- Arshian, A. H., & Morgenthal, G. (2017). Probabilistic assessment of the ultimate load-bearing capacity in laterally restrained two-way reinforced concrete slabs. *Engineering Structures*, 150, 52–63.
- Caltrans. (1994). *Memo to designers 7–1 (Bridge Bearings)*. California Department of Transportation.
- CEB-FIP (1991). Model code 1990. Comité Euro-International Du Béton, Paris, 87–109.
- DIANA. (2012). *Diana finite element analysis user's manual release 9.4.4*. DIANA.
- Fanning, P. J., & Boothby, T. E. (2001). Three-dimensional modelling and full-scale testing of stone arch bridges. *Computers & Structures*, 79(29–30), 2645–2662.
- Hordijk, D. A. (1991). *Local approach to fatigue of concrete, doctor dissertation*. Delft University of Technology.
- Huang, Z. Y., Wang, J. Y., Liew, J. R., & Marshall, P. W. (2015). Lightweight steel–concrete–steel sandwich composite shell subject to punching shear. *Ocean Engineering*, 102, 146–161.
- Kang, S. B., & Tan, K. H. (2016). Analytical model for compressive arch action in horizontally restrained beam-column subassemblages. *ACI Structural Journal*. <https://doi.org/10.14359/51688629>
- Keyvani, L., Sasani, M., & Mirzaei, Y. (2014). Compressive membrane action in progressive collapse resistance of RC flat plates. *Engineering Structures*, 59, 554–564.
- Korean Highway Bridge Design code (Limit state design). (2015). *Korea Road and Transportation Association*. Ministry of Land, Transport and Maritime Affairs.
- IT MIDAS. (2012). *MIDAS FEA Ver. 3.4.0 Manual. Manual of Midas IT* (pp. 225–290). MIDAS Information Technology Co., Ltd.
- Ministry of Land, Infrastructure and Transport (MOLIT). (2020). *Yearbook of road bridge and tunnel statistics*. MOLIT.
- Ohura, T., & Kato, M. (1993). Erection and field test of concrete arch bridge applying composite tube. *Journal of Construction Engineering and Management*, 119(4), 666–680.
- Oldrieve, W. (1915). *The ancient roof of Glasgow cathedral: Its condition and restoration* (Vol. 50, pp. 155–172). Proceedings of the Society of Antiquaries of Scotland.
- Peng, Z., Orton, S. L., Liu, J., & Tian, Y. (2017). Effects of in-plane restraint on progression of collapse in flat-plate structures. *Journal of Performance of Constructed Facilities*, 31(3), 04016112.
- Rankin, G. I. B., & Long, A. E. (1997). Arching action strength enhancement in laterally restrained slab strips. *Proceedings of the Institution of Civil Engineers-Structures and Buildings*, 122(4), 461–467.
- Selby, R. G., & Vecchio, F. J. 1993. *Three dimensional constitutive relations for reinforced concrete*. Department of Civil Engineering, University of Toronto, Toronto, Ont., Publication No. 93-02.
- Shukry, M. E. S., & Goode, C. D. (1990). Punching shear strength of composite construction. *Structural Journal*, 87(1), 12–22.
- Thorenfeldt, E. (1987). *Mechanical properties of high-strength concrete and applications in design*. Symposium Proceedings Utilization of High-Strength Concrete.
- Vecchio, F. J., & Collins, M. P. (1986). The modified compression-field theory for reinforced concrete elements subjected to shear. *ACI Journal*, 83(2), 219–231.
- Wang, S., Peng, J., & Kang, S. B. (2019). Evaluation of compressive arch action of reinforced concrete beams and development of design method. *Engineering Structures*, 191, 479–492.
- Yan, J. B., Liew, J. R., Zhang, M. H., & Li, Z. X. (2016). Punching shear resistance of steel–concrete–steel sandwich composite shell structure. *Engineering Structures*, 117, 470–485.
- Yang, D. H., Kwon, M. J., Eom, G. H., & Kim, J. H. J. (2018). RC arch deck development and performance evaluation for enhanced deck width. *International Journal of Concrete Structures and Materials*, 12(1), 60.
- Yu, J., & Tan, K. H. (2014). Analytical model for the capacity of compressive arch action of reinforced concrete sub-assemblages. *Magazine of Concrete Research*, 66(3), 109–126.
- Zheng, Y., Li, C., & Yu, G. (2012). Investigation of structural behaviours of laterally restrained GFRP reinforced concrete slabs. *Composites Part B: Engineering*, 43(3), 1586–1597.

Publisher's Note

Springer Nature remains neutral with regard to jurisdictional claims in published maps and institutional affiliations.

Submit your manuscript to a SpringerOpen® journal and benefit from:

- Convenient online submission
- Rigorous peer review
- Open access: articles freely available online
- High visibility within the field
- Retaining the copyright to your article

Submit your next manuscript at ► [springeropen.com](https://www.springeropen.com)